Corrosion Behavior of Calcium Containing 5xxx/6xxx Aluminum Alloys

A Thesis

Presented in Partial Fulfillment of the Requirements for the

Degree of Master of Science

with a

Major in Materials Science and Engineering

in the

College of Graduate Studies

University of Idaho

by

Saugat M. Singh

Major Professor: Dr. Batric Pesic, Ph.D.

Committee Members: Dr. Samrat Chaudhury, Ph.D., Dr. Gabriel Potirniche, Ph.D.

Department Administrator: Dr. Indrajit Charit, Ph.D.

December 2020

Authorization to Submit Thesis

This thesis of Saugat M. Singh, submitted for the degree of Master of Science with a major in Materials Science and Engineering and titled "Corrosion Behavior of Calcium Containing 5xxx/6xxx Aluminum Alloys," has been reviewed in final form. Permission, as indicated by the signatures and dates below, is now granted to submit final copies to the College of Graduate Studies for approval.

Major Professor: _____ Date: _____
Batric Pesic, Ph.D.

Committee Members: _____ Date: _____
Samrat Chaudhury, Ph.D.

_____ Date: _____
Gabriel Potirniche, Ph.D.

Department
Administrator: _____ Date: _____
Indrajit Charit, Ph.D.

Abstract

Aluminum alloys containing magnesium and silicon as main alloying elements are used for automotive applications. During the casting process, calcium can be a trace element or is introduced through deliberate addition. The addition of calcium may influence the corrosion properties of the alloy and introduce microstructural and compositional changes. This study investigates the potential effects of added calcium in corrosion behavior of as-cast, heat treated and rolled 5xxx and 6xxx Al alloys using standard corrosion evaluation techniques, like Tafel and cyclic polarization. Trace amount of calcium showed minimal effect on the corrosion behavior of the Al alloys, however it introduced modifications to the microstructure of 6xxx Al alloys. The as-cast 5xxx alloys showed improved passivity compared to the homogenized samples. During the heat treatment procedure, the size and distribution of intermetallic particle can disrupt the protective oxide layer lowering the corrosion resistance in homogenized alloys. Both 5xxx and 6xxx Al alloys showed susceptibility towards pitting corrosion. The as-cast 6xxx Al alloys showed increased susceptibility towards localized pitting corrosion with pits initiating at the center of the cell. This has been attributed to the inhomogeneous distribution of solute elements such as Si and Mg within the grain and their electrochemical difference with the Al-matrix. The effect of sensitization on corrosion behavior of 5xxx Al alloys was also studied. The 5xxx Al alloy showed slight improvement in corrosion behavior with increasing sensitization time up to 100 hrs. The corrosion behavior of the rolled Al alloys did not show significant differences compared to the cast Al alloys.

Acknowledgements

First and foremost, I would like to show my gratitude towards the funding and knowledge provided by NOVELIS Inc. I extend my thanks towards my major professor, Dr. Batric Pesic. Without his guidance and encouragement, this study would not have been possible. I am grateful for his patience, time, and his mentorship throughout the project.

My project would not have made progress without the technical input, persistence, and suggestions from Dr. Kumar Sundaram. I am thankful towards the support and assistance from Dr. Wu Zhang. I would also like to thank Dr. Indrajit Charit for his assistance and equipment in the project.

Dedication

This thesis is dedicated to my parents and my cousins Kalisha, Ruby, Ravi and Rajbin. I am grateful for my friends Lokendra, Rabindra, Nikunja, Bishal, Sajja and Saurav for their continuous support, entertainment, and encouragement. Finally, I would like to express my gratitude towards all my friends over the years who directly or indirectly played a role in helping me finish my thesis.

Table of Contents

List of Figures

List of Tables

List of Abbreviations

5xxx Ca H	Al 5xxx alloy homogenized with Ca.
5xxx H	Al 5xxx alloy homogenized.
5xxx Ca	Al 5xxx alloy as-cast with Ca.
5xxx	Al 5xxx as-cast alloy.
6xxx Ca H	Al 6xxx alloy homogenized with Ca.
6xxx H	Al 6xxx alloy homogenized.
6xxx Ca	Al 6xxx alloy as-cast with Ca.
6xxx	Al 6xxx as-cast alloy.
E vs Ag/AgCl	Potential collected with reference to Ag/AgCl electrode in Volts (V).
E_{corr}	Corrosion potential in Volts (V).
E_{ptp}	Pit transition potential in Volts (V).
log i	Current density in A/cm^2.
I_{corr}	Corrosion current in A/cm^2.
I_{ptp}	Pit transition current in A/cm^2.
AR	As-received alloy.
IGC	Intergranular corrosion.
CE	Counter electrode.
RE	Reference electrode.
WE	Working electrode.

Chapter 1: Introduction

1.1 Objectives

Al-Mg-Si alloys based on their chemical composition and thermal processing can be tailored for various automotive applications. 5xxx series aluminum alloys are suitable for inner-frame component whereas heat treatable 6xxx series aluminum alloys are generally used in extrusions and outer body sheet applications [1]. Al-Mg-Si alloys have great engineering applications with their excellent mechanical properties such as a good strength-to-weight ratio, good castability, low density, and good formability.

1 Rising levels of calcium (Ca) has been reported to modify the eutectic silicon in Al-Si alloys [2]. The addition of calcium may influence microstructural changes such as grain size and compositional chemistry. Additionally, possible changes in microstructure may alter the corrosion behavior of the aluminum alloy. The scope of this work includes the investigation of potential effects of trace calcium in the corrosion behavior and microstructural changes.

2 Homogenization heat treatment of the 5xxx and 6xxx Al alloys provides metallurgical significance in mechanical and chemical properties of the aluminum product after further processing during rolling. The microstructure evolution of commercial 5xxx and 6xxx Al alloys have been studied extensively. As-cast microstructures show a eutectic morphology and irregular compositions whereas with homogenization heat treatment, microstructures changes with a more finer grain size, compositional homogeneity, leading to dissolution of eutectic phases. The temperatures and heat treatment procedure alters the microstructure of the alloy as well as its chemical properties. These microstructural and compositional change can lead to the modification of intermetallic size/ratio, grain size, introduce compositional segregation, and the electrochemical activity of the alloy. The aim of this study is to investigate the modifications in the corrosion behavior of as-cast, homogenized, and rolled 5xxx and 6xxx Al alloys.

1.2 Literature Review

1.2.1 Thermodynamics of Aluminum in Aqueous Solutions

The corrosion process is electrochemical comprised of oxidation and reduction half-cell reactions. A reactant initially at equilibrium with standard potential (E^0), can be shifted towards the oxidation or reduction reaction. This shift in electrochemical potential during the reaction can be related with the change in Gibbs free energy. The various reactions involved during the corrosion process at various pH conditions can be described through the Pourbaix diagram in Figure 1.1 representing the various electrochemical reactions involved. The Pourbaix diagram or the Eh-pH diagram represents the thermodynamic stability of the aluminum alloy in a specific environment. These lines in the figure are constructed based off the Nernst equation below. Each line represents the stability of aluminum and speciation as a function of pH.

$$E = E^0 + 2.3\frac{RT}{nF}\log\frac{[B]^b[H_2O]^d}{[A]^a[H^+]^m} \quad (1)$$

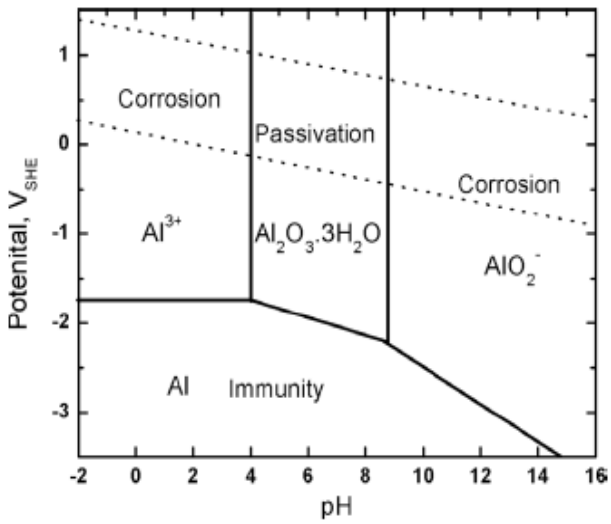

Figure 1.1: Eh-pH diagram of pure Al at 25°C in aqueous solution [3].

where, E is the potential, E^0 is the standard potential, n is the number of electrons exchanged during the reaction, F is the Faraday constant, R is the gas constant, T is the temperature, n is the number of electrons, m and d are molar constants of reactants (A) and products (B) respectively. It is seen that Al has its passivity range within pH 4-9 by the formation of Al_2O_3 film. At lower pH or acidic environment, Al is oxidized to Al^{3+} while AlO^{2-} is formed in the higher pH range or the alkaline region [3]. With the

use of electrochemical polarization techniques, information on the corrosion kinetics, passivation, and corrosion rate can be obtained.

1.2.2 Kinetics of Electrochemical Reactions

The Butler-Volmer equation below describes the relationship between current density and applied potential. For a given reversible reaction, the half-cell reactions are as follows:

$$2H^+ + 2e^- \rightarrow H_2 \tag{2}$$

$$H_2 \rightarrow 2H^+ + 2e^- \tag{3}$$

At equilibrium, the half-cell electrode potential e_{H^+/H_2}. When an overpotential is applied, an energy barrier is created for the forward and backward reaction. This activation energy difference is given by ΔG_f and ΔG_r , corresponding to the forward and backward scans respectively and are shown in the energy model in the activation overpotential in Fig 2a. The difference in activation energy difference is related to the half-cell electrode potential given by,

$$\Delta G_f - \Delta G_r = -nFe_{H^+/H_2} \tag{4}$$

From the Maxwell distribution law, the forward and reverse reaction rates are given by,

$$r_f = K_f e^{\frac{\Delta G_f}{RT}} \tag{5}$$

$$r_r = K_r e^{-\frac{\Delta G_r}{RT}} \tag{6}$$

where K_f and K_r are reaction rate constants for the forward and backward reactions. Electrochemical reactions involve the loss or gain of electrons so the rate of reactions can be a measure of the current. Then at equilibrium, according to Faraday's law, the proportionality between mass reacted and electron flow measured in current i_o gives the reaction rate,

$$r_f = r_r = \frac{i_o a}{nF} \tag{7}$$

where a is the atomic weight. Subsequently, when cathodic overpotential is applied, activation energy of the discharge reaction is reduced by the amount $\alpha nF\eta$ and for the ionization reaction, increasing the rate by $-(1-\alpha)nF\eta$. Here, η is the activation polarization or overpotential, α and (1- α) are fractions of η taken by discharge and ionization (forward and reverse) reactions, respectively. Then the Butler Volmer equation gives the net applied current in terms of current density becomes,

$$i = i_c - i_a = i_o[e^{\frac{\alpha nF\eta}{RT}} - e^{\frac{-(1-\alpha)nF\eta}{RT}}] \quad (8)$$

where i_c and i_a are the cathodic and anodic current density from the applied potential, i_o is the exchange current density. When a large overpotential is applied to the metal electrode, in case of a negative overpotential, the first term in Equation 8 becomes negligible.

$$i = i_o e^{\frac{-\alpha nF\eta}{RT}} \quad (9)$$

Taking the log on both sides,

$$\ln i = \ln i_o - \frac{\alpha nF\eta}{RT} \quad (10)$$

In the case of a positive overpotential, the second term is negligible. In the case Equation 2 reduces to the following linear equation,

$$\ln i = \ln i_o + \frac{(1-\alpha)nF\eta}{RT} \quad (11)$$

When the current density i is plotted against the overpotential η, two linear regions can be identified by Equation 10 and 11 above. The slope of these lines in Equation 10 and Equation 11 as seen in Figure 1.2 represent the cathodic and anodic Tafel slopes, respectively.

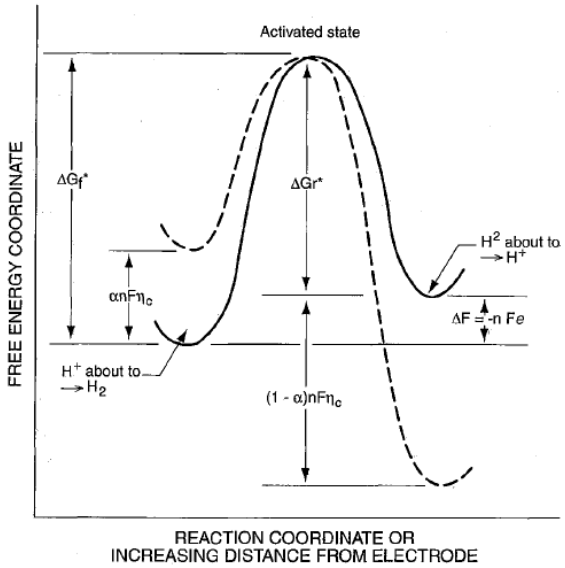

Figure 1.2: Activation energy model for activation overpotential. Equilibrium state indicated by solid line; polarized state indicated by dashed line [3].

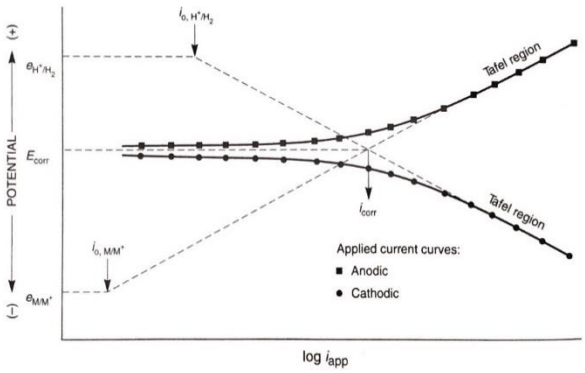

Figure 1.3: Corrosion behavior described through Tafel plot [3].

Polarization tests such as Tafel polarization utilize applied voltage as means for driving the reaction while changes in current are measured. Polarization studies are advantageous to other corrosion weight loss techniques as it can be conducted at a short time in a non-destructive fashion. During the Tafel polarization, potential is applied to the range of ±250 mV in the cathodic (negative potentials) and anodic (more noble potentials) from equilibrium. The Open Circuit Potential (OCP) describes the equilibrium potential for the metal-electrolyte system without any applied current. OCP can also be interpreted as the thermodynamic parameter indicating the tendency towards corrosion activity. Since the tests are run

near the equilibrium state, current changes are measured in the micro-amps range. The two branches in the Tafel plot represent the cathodic and anodic half reactions. The intersection of these two branches specifies the corrosion potential (E_{corr}) and corrosion current density (i_{corr}) as seen on Figure 1.3. Here, β_a and β_b are slopes of the linear region in the cathodic and anodic branches, respectively [3].

1.2.3 Localized Corrosion: Pitting Corrosion

The passive aluminum oxide inhibits the oxidation of the underlying metal, however, in an aggressive Cl^- environment, the film becomes unstable, degrades due to the Cl^- attack [4]. A localized attack can occur in the form of shallow holes, deep penetrations in different shapes. This type of corrosion is referred to as pitting corrosion [4,5]. Pits can be metastable, stable and can even propagate into deeper pits.

The mechanism that lead to the stages of pitting corrosion have been discussed by many authors yet there is still no consensus [3, 4, 5, 6]. Natishan and O'Grady [4] reviewed the theories regarding pit initiation and categorize pit initiation into the following steps: i) Ion migration / penetration of the oxide ii) Adsorption / ion displacement leading to oxide thinning iii) Breakdown of the oxide layer.

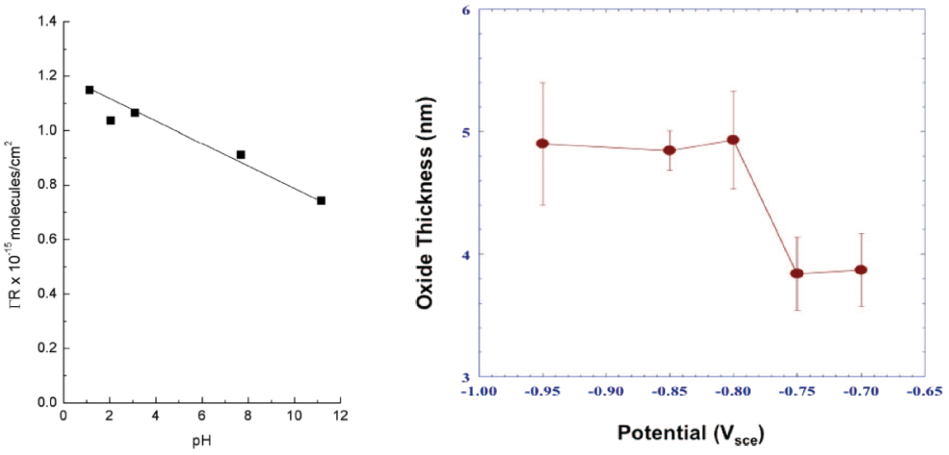

Figure 1.4: a) pH dependence of chloride adsorption on aluminum (τR is the surface concentration of the radioactive isotope) in 0.1M $NaClO_4$ **b)** XPS-derived thickness measurements of oxides on polycrystalline Al (99.9995% Al) samples, which were anodically polarized in de-aerated 0.1 M NaCl solution at room temperature [4].

When the Al alloy is exposed to NaCl solution, the adsorption of Cl^- by the oxide film is attributed to the attractive forces. The isoelectric point (pH with no electric charge) of the oxyhydroxide (AlOOH)

layer is ~9 which attracts anions such as Cl^- in the aqueous solutions to the surface providing opportunity for interaction. At increasing pH, the adsorption of Cl^- is reduced as seen in Fig 3a. Several surface analysis techniques suggested that adsorbed Cl^- then penetrates through the oxide film reducing its thickness. In Fig 3b, the variation in oxide thickness in 0.1 M NaCl is measured with the change in potential. The oxide thickness remains consistent until it reaches -0.8 V_{SCE} and then the thickness decreases at higher potentials. Past this potential, the chloride is incorporated into the film and can interact with the bulk metal [4].

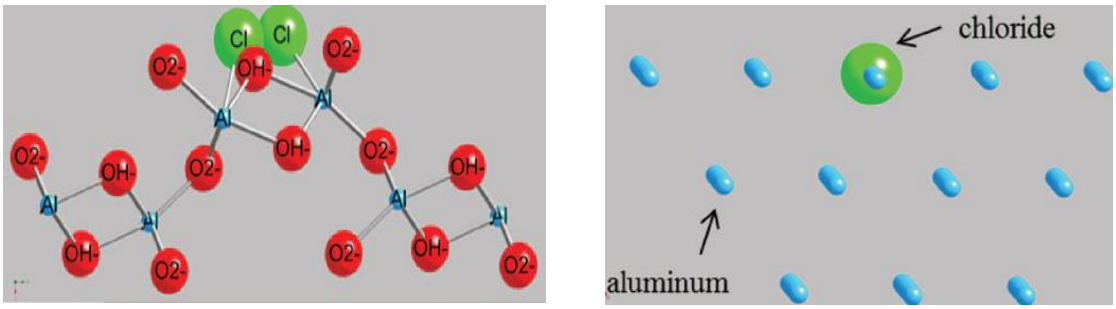

Figure 1.5: a) Model illustrates two Cl- substitutes for one elevated OH- site **b)** Model depicts a chloride ion in the site of an aluminum atom in the (111) surface plane [4].

Using modeling and surface analysis technologies, Natishan and O'Grady [4] proposed a model for Cl^- interaction with the bulk Al surface. At the pitting potential, both recessed and elevated sites in the oxide film (Figure 1.5a) are under attack. Further past a certain potential, the Cl^- is now incorporated a^{111} surface plane (Figure 1.5b) and the oxide metal interface and interacts with the metal surface.

Once the pitting has initiated the electrochemical process can be separated to the anodic and cathodic parts. The schematic of pitting corrosion is shown in Figure 1.6 below. The anodic reaction in the electrochemical process involves the oxidation of the metal as it is removed from the alloy.

$$Al \rightarrow Al^{3+} + 3e^- \tag{13}$$

Similarly, the cathodic process involves the reduction process of dissolved oxygen in water in cathodic sites.

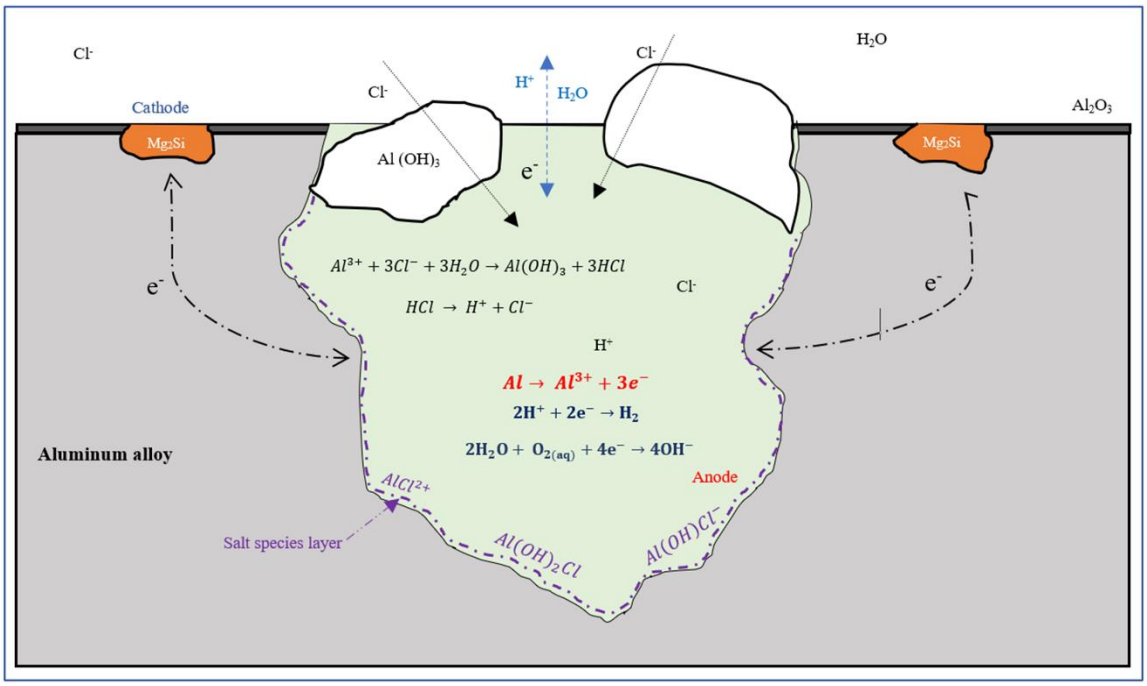

Figure 1.6: Schematic representation of pitting activity of aluminum alloy in chloride containing solution [4].

$$2H_2O + O_{2(aq)} + 4e^- \rightarrow 4OH^- \quad (14)$$

$$2H^+ + 2e^- \rightarrow H_2 \quad (15)$$

If the cathodic area is bigger than the anodic side, the anodic current density will be higher than the cathodic, resulting in a greater anodic dissolution of metal. Several authors [7,15,12] agree that Cl^- interacts with the Al^{3+} to form aluminum oxychloride intermediates such as $Al(OH)Cl_2$ and $Al(OH)_2Cl$ in the following Equation 16-19. However, these intermediates are unstable and more soluble, and addition of stirring and dissolved oxygen can accelerate the damage to the salt layer in the pit geometry.

$$Al^{3+} + H_2O \rightarrow Al(OH)_2^+ \quad (16)$$

$$Al^{3+} + Cl^- \rightarrow AlCl^{2+} \quad (17)$$

$$Al(OH)_2^+ + Cl^- \rightarrow Al(OH)Cl^- \quad (18)$$

$$AlCl^{2+} + 2H_2O \rightarrow Al(OH)_2Cl + 2H^+ \quad (19)$$

The aluminum further can react with the Cl^- ions in the solution and with the pH is lowered with the introduction of hydrochloric acid in Equation 20. From the Pourbaix diagram in Figure 1.1, we can see that lower pH introduces Al^{3+}, which reacts with the chloride ion and forms aluminum hydroxide.

$$Al^{3+} + 3Cl^- + 3H_2O \rightarrow Al(OH)_3 + 3HCl \quad (20)$$

The aluminum hydroxide formed during the process forms an insoluble cap at the pit mouth. The cap is porous enough to let the Cl^- into the pit solution. The acidification further promotes the dissolution of the metal matrix and the pitting process becomes autocatalytic [5].

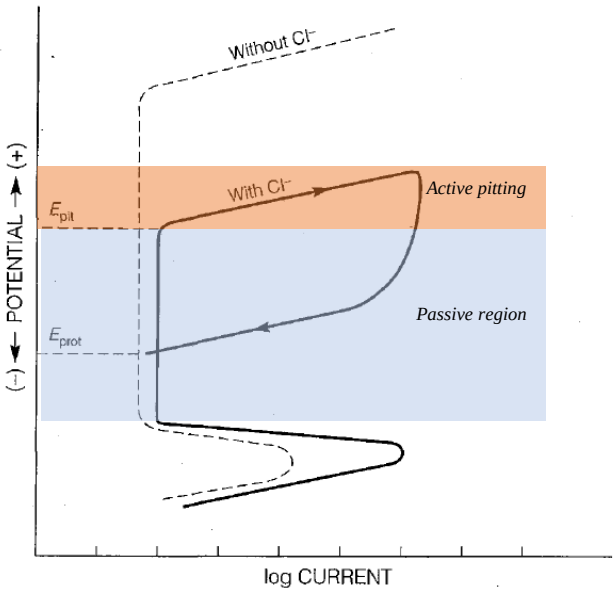

Figure 1.7: Schematic of typical anodic cyclic potentiodynamic polarization curves analog to steel [3].

Cyclic polarization can be used to estimate the extent of localized corrosion. In Figure 1.7, the alloy passivates (in the case of Fe), where the polarization scan remains fixed at a specific current over a range

of potential until it reaches the breakdown or pitting potential. Electrochemically, pitting can be characterized by the pitting potential (E_{pit}) during the forward scan in the anodic direction in Figure 1.8. A more noble E_{pit} shows better resistance towards pitting corrosion. These pits initiate past the pitting potential (E_{pit}) where the current rises rapidly due to the anodic dissolution of the aluminum matrix [5,6,8].

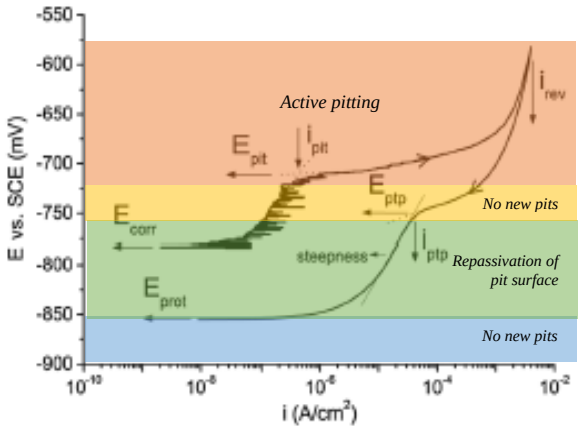

Figure 1.8: Schematic representation of the characteristic parameters of pitting and repassivation processes in Al 6082 in 0.6 M NaCl [8].

After some degree of anodic polarization in the forward scan, the direction is reversed in the cyclic polarization test. During this return scan, a hysteresis is formed if the scan moves towards lower potentials. If the scan moves towards a positive direction and shows no hysteresis, the alloy is resistant towards pitting. However, in the Al alloy, a hysteresis is observed suggesting propensity towards localized corrosion. The use of single cycle repassivation, also referred as pitting scan has been carried out 1) to estimate the susceptibility of localized corrosion in aggressive environment such as chloride and 2) providing qualitative indication of localized attack. During the reverse scan of the cyclic polarization process, an inflection is observed in aluminum alloys (at E_{ptp} and i_{ptp}) seen in Figure 1.7. The pit transition potential (E_{ptp}) is the thermodynamic driving force for Al dissolution in the acidified pit when it meets the newly repassivated fresh surface. [9] Eptp has also been considered as a long-term indicator of localized corrosion [10]. Yasuda et. al. [11] also reported that the E_{ptp} is independent of original surface orientation and amount of pit growth. Shukla et. al. [10] suggested that the increase of prior corrosion show a decrease in E_{ptp}. While potentials higher than E_{pit} is indicative of the onset of pitting, repassivation occurs past E_{ptp}. With higher values of E_{pit}, the metal is more resistant to pitting whereas with higher values E_{ptp}, metals can repassivate. Localized corrosion can propagate between the potentials of E_{pit} and E_{ptp}. The current density at the inflection point (i_{ptp}) is the rate at which hydrolysis

equilibrium is reached at a critical saturation concentration of Al^{3+} [12]. According to Pickering et. al [13], the transition is prominent due to i) limited mass transfer between the pit and the bulk solution ii) evolution of hydrogen during the pitting process [15, 11, 13]. The steep decrease in potential past E_{ptp} can be attributed to the difficulty in simultaneous repassivation in a more occluded geometry of pits (mouth of the pit narrower than pit cavity) rather than repassivation of all corroded surfaces. Assuming stagnant conditions, and processes depending on concentrations of Al^{3+} and Cl^- only, the effective anodic charge transfer coefficient α_{eff} can be determined through the method developed by Engelhardt et. al [14].

$$\ln \frac{i}{i_{ptp}} = \frac{\alpha_{eff} F}{RT} (E - E_{ptp}) \tag{21}$$

F, R and T have usual designation defined above from Equation 1. α_{eff} can be used to estimate the contribution of electromigration of Cl^- for the compensation of potential drop. From Equation 21, the steepness of the repassivation curve past E_{ptp} can be used to estimate $\alpha_{eff.}$ Furthermore, decrease in α_{eff} estimates corresponds to increase in the potential gradient and subsequent acceleration of Cl^- migration. The steepness of potential decrease can be used as a function of log (Cl^-) to determine the repassivation kinetics [14,15]. The reverse scan then reaches the crossover potential E_{prot} at the intersection of the forward and reverse scan, below which no new pits are formed. The width of the hysteresis $\Delta E = E_{pit} - E_{prot}$ can then been used to as an indication of the propensity of localized corrosion [15].

1.2.4 Localized Corrosion: Intergranular Corrosion

Intergranular corrosion (IGC) is a severe attack along the grain boundaries (GB) or the vicinities of the grain boundaries. The electrochemical difference between the precipitation at the grain boundary and the precipitate free zones can drive the IGC. The more anodic metal is first to dissolve actively, which may lead to cracks along the grain boundary or through the grains.

Susceptibility to corrosion in the 6xxx series Al alloys is dependent on the balance of Mg/Si ratio required for the formation of Mg_2Si. The excess silicon added tends to segregate along the grain boundaries, and acts as an effective cathode promoting intergranular corrosion [8]. In the case of the 5xxx series alloys, enrichment in magnesium offers excellent strength and formability in combination

with other alloying elements such as manganese, chromium, and iron. Magnesium has higher solubility in aluminum around 14.9 wt% at 450°C however the solubility reduced to around 1.7 wt% at room temperature. This reduction in solubility leads to a supersaturated solid solution (SSSS) α-matrix of aluminum and magnesium. Alloys containing more than 3wt% Mg exposed to a longer period at temperature lower than 150°C tend to diffuse from the SSSS and precipitate into lower energy sites such as grain boundaries. Precipitation of β-phase (Al_3Mg_2) has been deleterious in the intergranular susceptibility of the alloys because the potential difference between the β-phase and the α-matrix provides a driving force for anodic dissolution [16].

The chemistry of the 5xxx and 6xxx series alloys lead to some complex microstructures with precipitates based on their thermal history. Various intermetallic particles (constituents, dispersoids and precipitates) may lead to localized corrosion and damage to the alloy. The electrochemical interactions between the particle formed and the aluminum matrix is essential to understand the IGC in the alloy [5]. Some of the typical intermetallics present in the aluminum alloy and their electrochemical activity is described in Table 1.1 below. Pit initiation and propagation may result in dissolution of second-phase particles, which may alter the electrochemical activity leading to an acceleration of IGC. The particle induced corrosion is like galvanic corrosion, where the mutual differences between electrochemical behaviors leads to IGC. Each particle may exhibit distinctive electrochemical property with respect to the matrix. To evaluate the corrosion activity, the electrochemical activity of the intermetallic must be compared. Intermetallic with more noble potential will act as a cathode and will support the cathodic process while more anodic particles will actively corrode. Local galvanic cells may support cathodic or anodic reactions providing a driving force for corrosion.

The addition of manganese (Mn) has been reported to modify the microstructure by forming a series of second-phase particles such as Al_6MnFe, equal to the electrochemical potential of Al matrix. Addition of Mn is reported to decrease pitting susceptibility of Al alloys by modification of Fe containing intermetallic particles [5]. Addition of silicon in Al-Mg-Si alloys have shown to improve the mechanical properties of the alloy by the formation of Mg_2Si. Any silicon in excess, introduces Si along the grain boundaries causing the initiation of IGC [16].

Table 1.1: Corrosion potential of active intermetallics [5].

Intermetallic	Corrosion potential V vs SCE
Al_3Fe	-0.539
Al_6Mn	-0.779
Al_3Mg_2	-1.013
Mg_2Si	-1.538

Studies by Zhang et. al. [17] showed that the electrochemical differences between intermetallic in 6xxx series alloys such as Mg_2Si, Si and Al matrix can lead to both IGC and pitting in a corrosive environment. With mole ratios between Mg to Si higher than 1.73, Si may even precipitate near the grain boundaries. Initially, Mg_2Si is seen to be electrochemically negative compared to the Al matrix and Si. As the alloy is exposed to corrosive environment, Si acts as a cathodic zone; Mg_2Si however, is seen to preferentially dissolve, resulting in an enrichment of Si along the grain boundary. This solid-state dissolution causes a shift in electrochemical activity of Mg_2Si from initial anodic potential to more positive direction leading to anodic dissolution of the Al matrix near the Mg_2Si phase. Both Mg_2Si and Si initiate corrosion near the precipitate free zones. [17,18]

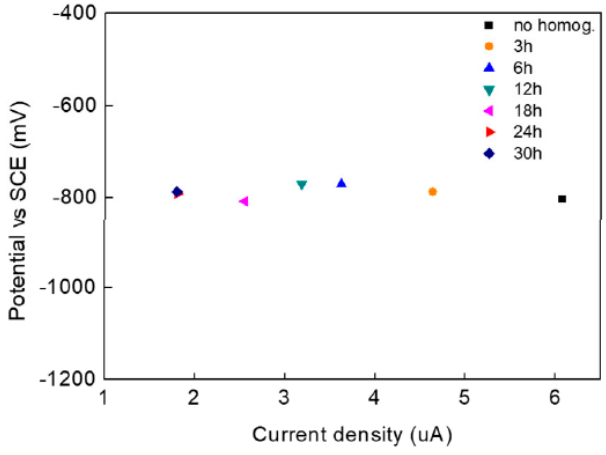

Figure 1.9: Changes in corrosion potential and current with increase in homogenization time [19].

Studies by Choi et. al. [19] explored the changes in corrosion behavior in Al-Mg alloys as a function of homogenization heat treatment time. Homogenization carried out at 450°C shows improvement in corrosion resistance with increase in the homogenization time as seen in Figure 1.9. With increase in homogenization time, the magnesium content along GB decreases while Si and Mg_2Si content increase along GB. With Si high cathodic reduction potential, Mg_2Si act as a sacrificial anode, leading to the decrease in corrosion rate. However, in the present study, such significant changes in the corrosion current was not seen. The homogenization process and compositional changes may be specific to an alloy and corrosion behavior may have altered accordingly. Additionally, the corrosion current was used as an indicate only the surface corrosion, and localized corrosion such as pitting was not considered. Although changes in as-cast, homogenized and rolled alloys bring microstructural changes, the changes in corrosion behavior has not studied as much.

1.3 Addition of Trace Amount of Calcium

Kumari et al. [20], Ludwig et al. [21], and Lim et al. [22], suggested that rising levels of Ca modify the eutectic Si and increase the porosity in Al alloys. In Al-Si alloys, the eutectic Si solidify as fibrous-like structure, but in the presence of Ca element the eutectic Si solidify as acicular flake-like structure resulting in improved strength and fracture toughness of the alloy. In addition, Ca in ranges of 0.02 to 0.05 % results in modification of Fe-rich intermetallic improving the mechanical properties of the alloy. The mechanism of refinement has been attributed to the increase in growth velocity of Si phase, while trace Ca causes reduction in the eutectic Al nucleation rate. The addition of Ca may influence the corrosion properties of the alloy via changes such as microstructure, grain size and compositional chemistry. Gupta, et al. [23] observed that addition of 0.08 wt.% Sr decreased the intergranular corrosion of a 5xxx Al alloy by more than 60%, assigning this phenomenon to the decrease of β-phase at grain boundary. Because Sr and Ca have similar affinity toward aluminum, the idea born was to explore if the presence of Ca would produce similar effects.

Chapter 2: Experimental Procedure

2.1 Material Preparation

Table 2.1 shows the composition of alloys used in this study. The alloys were prepared using 90kg heat resistance melting furnace, clay graphite crucible, high purity Al, and commercial master alloys. Just before casting, the alloy melt was degassed with argon, and Al-3Ti-1B grain refiner was added to the melt. The preheated trough coated with boron nitride was used to deliver the molten metal from the furnace to the direct chill (DC) casting pit. The ingot was cast using water hole mold of 89x228.6mm size. Only the steady state cast part of the ingots is used for the microstructural characterization and corrosion study.

Table 2.1: The chemical composition of the alloys (all in wt. %, unless otherwise stated).

Alloy	Si	Fe	Cu	Mn	Mg	Ti	Ca	Al
6xxx	0.8	0.26	0.09	0.08	0.64	0.013	0.0002	Bal.
5xxx	0.09	0.27	0.09	0.07	4.51	0.02	0.0002	Bal.
6xxx+ Ca	0.8	0.27	0.09	0.07	0.64	0.02	0.0058	Bal.
5xxx + Ca	0.09	0.26	0.07	0.44	4.5	0.02	0.005	Bal.
Rolled 6xxx-A	0.76	0.22	0.09	0.07	0.64	0.01	0.012	Bal.
Rolled 6xxx-B	0.82	0.25	0.09	0.11	0.62	0.03	0.003	Bal.
Rolled 5xxx	0.1	0.27	0.04	0.43	4.55	0.01	0.005	Bal.

Each ingot was subsequently cross sectioned along the casting direction into two halves. One of the blocks was used to prepare as-cast samples, and the other was used to prepare homogenized samples. A heat-resistant air-convection furnace was used for the homogenization heat treatment. A dummy block with thermocouple was also placed along with the actual sample in-order to record the thermal trace of the heat treatment. The 5xxx and 6xxx Al alloys were homogenized at 520±5°C for 16 hrs and at 555±5°C for 16 hrs, respectively. In all cases, the blocks were heated at 50°C/hr and cooled to room

temperature inside the furnace. From each block, 305x15mm cylindrical samples were produced for the corrosion test. The as-cast samples are referred as 5xxx, 5xxx+Ca, 6xxx and 6xxx+Ca, and the homogenized heat-treated samples are referred as 5xxx H, 5xxx+Ca H, 6xxx H and 6xxx+Ca H. The cylindrical samples were further cut into 12.7x15mm working electrodes (WE). A control sample of pure aluminum (99.99% Al) of diameter 15.7 mm (Figure 2.1) was prepared to compare the corrosion behavior with the alloys. Working electrodes of diameter 15.7 mm coins (Figure 2.2) were punched from the rolled aluminum sheets.

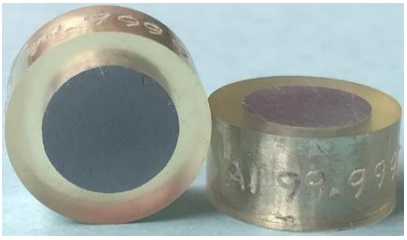

Figure 2.1: Pure Al (99.999%) working electrode sample.

Figure 2.2: Rolled Al working electrode samples.

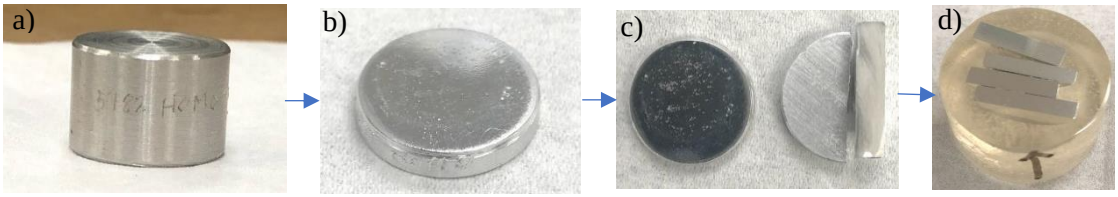

Figure 2.3: Cross section procedure: **a)** Cylindrical WE **b)** Top surface of WE **c)** Cross section of top surface **d)** Cold mount of cross section surfaces.

The samples were grounded and polished up to 0.05-micron colloidal silica with standard procedure for the microstructural investigation. The polished samples were anodized using Barker's reagent (1.8% fluoroboric acid in water) for 120 s at 20 V to reveal primary α-Al grains using Leica DM 4500 polarized

light microscopy and Media Cybernetics, Inc. image-Pro® plus software (version 4.1). The grain size and dendritic arm spacing (DAS) were measured using the line intercept method (ASTM E112). JMatPro (version 12) software with Al-DATA database was used to predict phases as a function of temperature.

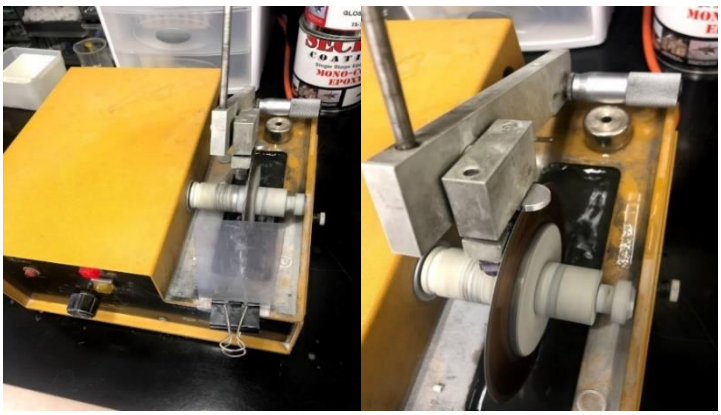

Figure 2.4: Low speed saw for cross section of the plate/coin working electrodes.

To study the cross sections of the corroded alloys, plates (diameter 15.7 mm; height 2.89 mm) were cut from the cylindrical working electrode. The plates were then corroded in the electrochemical cell with 0.6 M NaCl at pH 6.5. For the rolled alloys, cross sections were made along the rolling direction. The cross-section procedure is illustrated in Figure 2.3. A low speed saw was used to make the cross sections of the plate/coin samples as seen in Figure 2.2. The cross sections were then cold mounted and polished with 0.05-micron colloidal silica. The morphology of the corroded samples was examined using the Olympus Leco PMG3 inverted metallurgical optical microscope.

Figure 2.5: Lindberg/Blue tube furnace setup for solution heat treatment (SHT) of 5xxx alloys.

To study the effect of sensitization, the 5xxx H, 5xxx+Ca H and rolled 5xxx samples were further heat treated. The samples were placed in a Lindberg/Blue tube furnace for solution heat treatment (SHT) (shown in Figure 2.4) at 450°C for 1 hr and subsequently water quenched. Further aging heat treatment was carried out in the furnace by heating up the quenched samples to 150°C and maintaining at that temperature for 50 hr and 100 hr followed by cooling the samples in air.

2.2 Electrochemical Cell Setup

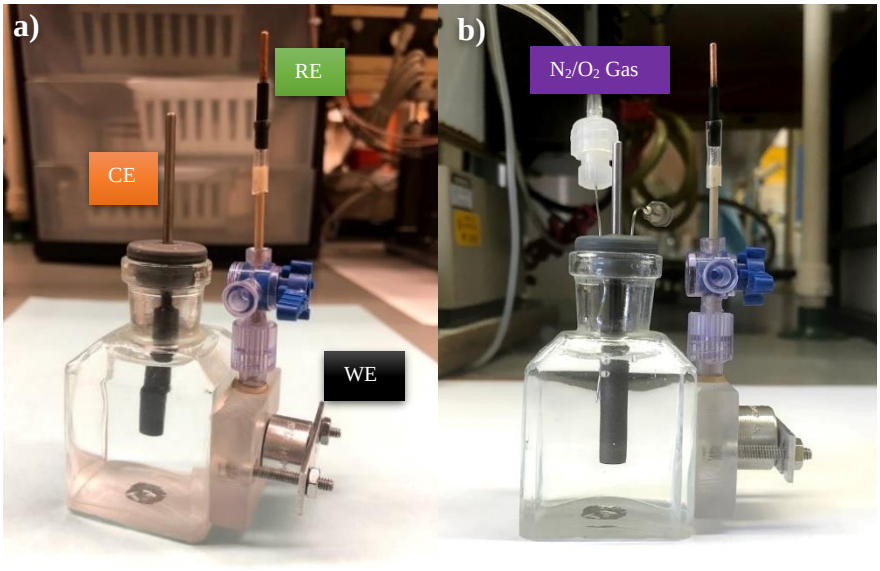

Figure 2.6: a) Electrochemical cell setup with Al as WE, Ag/AgCl as RE and graphite as CE **b)** Electrochemical cell setup with inlet for introduction of N_2 or O_2 for experimentation under controlled atmosphere.

In a three-electrode electrochemical cell, the aluminum alloy is used as the working electrode (WE), Ag/AgCl as the reference electrode (RE) and graphite as the counter electrode (CE) as seen in Figure 2.6. Electrochemical measurements were performed at room temperature with the WE area of 0.654 cm^2 area exposed to solution. The reference electrode was of a leak free type to avoid contamination by chloride ions by reference electrode filling the solution. Working electrode samples were polished and sonicated before each corrosion testing. The standard test solutions were reagent grade sodium chloride (NaCl) dissolved in deionized water adjusted to desired pH by using H_2SO_4 and NaOH. Electrochemical studies were performed by using the Princeton Applied Research EG&G Model 273A potentiostat-galvanostat. To study the effect of deaeration and oxygen saturation, a small needle was passed into the cell to introduce either nitrogen or oxygen. The gas was purged in solution for 15 min and the gas was kept above the solution during the electrochemical tests. The open circuit potential (OCP) was stabilized for 15 minutes by performing 30 CV scans were run at 200 mV/s and additional 5 minutes wait period. OCP was kept within 100 mV of each other between trials. The electrochemical tests were performed at a scan rate of 10 $mVmin^{-1}$. During the cyclic polarization (CP) tests, the scan was reversed when the anodic current reached a pre-selected current (i_{rev} = 2.5 x 10^{-3} Acm^{-2}). At least three repeated results were carried out in each test and the average results are represented in the following sections. The graphical analysis of the results was achieved through Originlab version 9.0.

Chapter 3: Results and Discussions

3.1 Electrochemical Studies

3.1.1 Effect of pH using Tafel Polarization on 5xxx Al Alloys

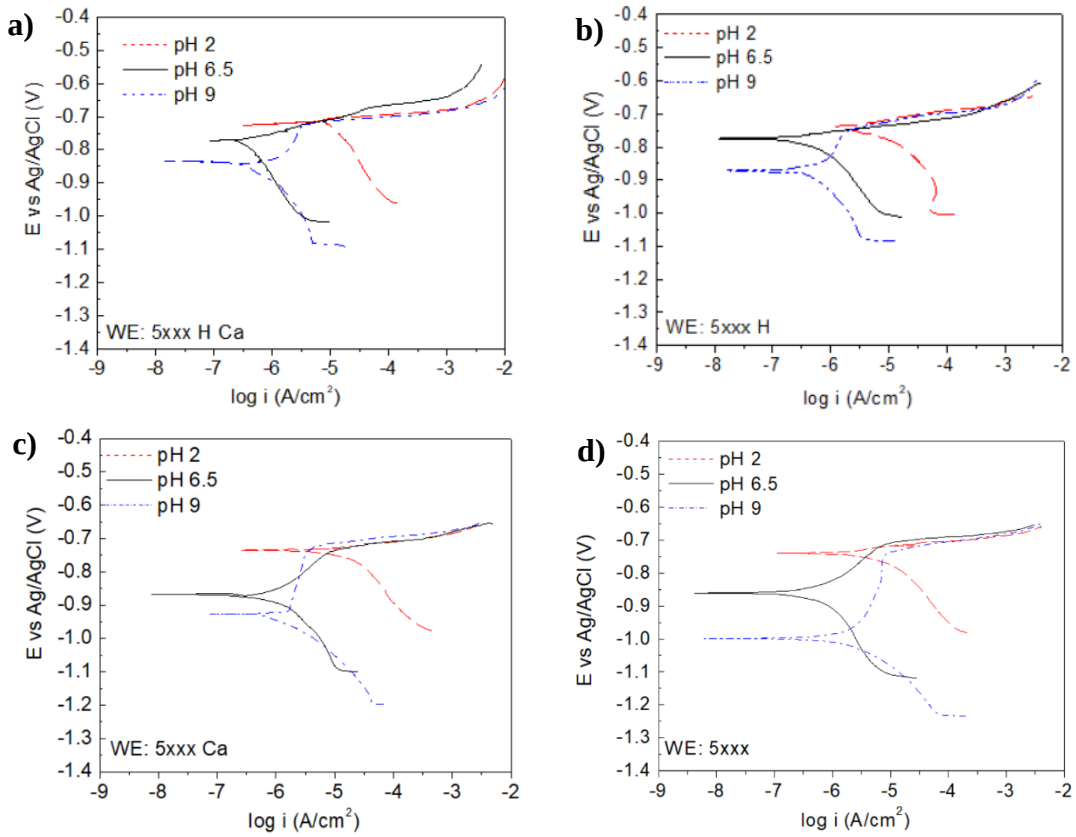

Figure 3.1: Effect of pH on the Tafel polarization of **a)** 5xxx HOMO Ca **b)** 5xxx HOMO **c)** 5xxx as-cast with Ca **d)** 5xxx as-cast.

The effect of pH can be seen through the Tafel behavior in Figure 3.1. Although the changes in composition and thermal treatment varies between alloys, the overall Tafel behavior is consistent. At lower pH 2 (battery acid), no passivity is observed due to high solubility of Al^{3+} ion in acidic solutions as seen in the Pourbaix diagram in Figure 1.1. As pH is increased to 6.5 (standard seawater condition), only a slight passivity is observed however the pitting potential remains consistent. Further increase in the pH, shows a decrease in the open circuit potential (OCP) leading to a lower E_{corr}. The formation of $Al(OH)_3$ at higher basic pH 9 (greater salt sea and soil pH in humid conditions) leads to this increase in

passivity however, as the corrosion progresses, pitting potential and the anodic slope is uninfluenced by the changes in pH.

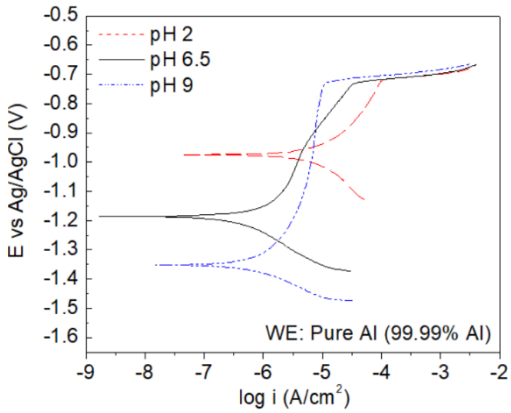

Figure 3.2: Effect of pH on the Tafel polarization of pure Al (99.999%) in 0.6 M NaCl.

A control sample of pure Al was used to compare with the Tafel behavior of the alloys. The E_{corr} of pure Al sample shifted to lower potentials and towards a more negative current density. This indicates that the alloyed samples having a more positive E_{corr} are more susceptible towards corrosion than pure Al. It can also be observed that there is a wider area for passivity in pure Al in all three pH changes as seen in Figure 3.2. This is due to the immediate formation of passive film on the Al surface. Addition of alloying elements can alter the passivation due to formation of precipitates/intermetallic and enhance the anodic behavior of the alloy [24]. The anodic and cathodic reaction during the aluminum corrosion are the dissolution of aluminum (Equation 13) and the reduction of dissolved oxygen (Equation 14). Aluminum hydroxide can be formed during through the process as seen in Equation 20. This aluminum hydroxide can further breakdown into aluminum hydroxide through the following equation.

$$2Al(OH)_3 \rightarrow Al_2O_3 + 3H_2O \tag{22}$$

The oxide film may not be sufficient during the chloride attack and could easily penetrate through the passive film inducing the aluminum dissolution. However, in the case of the aluminum alloy, formation of precipitates in the alloy can alter the formation of the oxide film and can act as active sites for pitting.

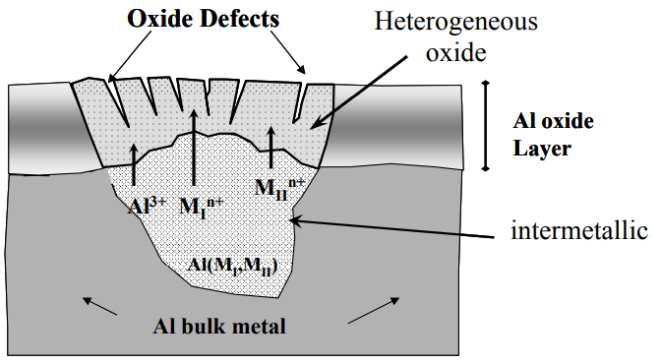

Figure 3.3: Effects of intermetallics on the oxide growth on aluminum alloys [23].

The formation of intermetallic phases might be beneficial in terms of the alloy's mechanical properties however its corrosion resistance is reduced. The metal solution interface consists of hydroxyl groups [24], whose acid-base properties determine the surface charge of the oxide layer. This surface charge is significant with its interaction with halide ions such as Cl^- [4,24]. The isoelectric point (pH with no electric charge, pH_{pzc}) with a net positive character on the surface can attract anions such as Cl^-. The net positive character of the surface has been represented by Flores [24] through the following Equation 23. In cases of higher pH than the pH_{pzc}, the surface has a net negative charge and the negative characteristic on the surface can be represented by Equation 24.

$$-\mathrm{MOH_{surf}} + \mathrm{H_{aq}^+} \rightarrow -\mathrm{MOH_{2\,surf}^+} \tag{23}$$

$$-\mathrm{MOH_{surf}} + \mathrm{OH^-} \rightarrow -\mathrm{MO_{surf}^-} + \mathrm{H_2O} \tag{24}$$

where, M represents the metal cation. Natishan and McCafferty [4] suggested that addition of alloying elements such as Si, Ti, Cr, W and Zr may alter the isoelectric point (pH with no electric charge). Alloys are less corrosion resistant compared to pure Al due to the following reasons. i) The positive net charge of aluminum is lowered which attracts anions like Cl^- in the aqueous solutions to the surface providing opportunity for interaction. Subsequently, the pitting potential of these alloying elements are much higher making aluminum more reactive in the aqueous media towards pitting corrosion. ii) Intermetallic also introduce defects and compositional changes in the oxide layer disrupting the continuous passive range. In addition, oxides formed on top of intermetallics are reported to be porous compared to the Al matrix. iii) The electrochemical difference between intermetallic particles and bulk Al matrix can drive the corrosion process. In the aqueous solution, these defects can act as weak points in the corrosion attack.

Table 3.1: Summary of Tafel data of 5xxx aluminum alloys and pure Al (99.99%) in 0.6 M NaCl at pH 6.5.

Alloy	pH	E_{corr} (V)	I_{corr} (A/cm^2)	βa (V/decade)	βc (V/decade)
5xxx+Ca H	2.0	-0.701	-4.883	0.013	-0.332
	6.5	-0.756	-6.192	0.036	-0.266
	9.0	-0.896	-5.922	0.402	0.247
5xxx H	2.0	-0.723	-5.128	0.028	-0.191
	6.5	-0.818	-6.122	0.087	-0.222
	9.0	-0.901	-6.264	0.295	-0.145
5xxx+Ca	2.0	-0.721	-4.724	0.013	-0.227
	6.5	-0.857	-5.974	0.159	-0.225
	9.0	-0.911	-5.772	0.588	-0.181
5xxx	2.0	-0.717	-5.096	0.011	-0.212
	6.5	-0.849	-6.069	0.147	-0.298
	9.0	-1.027	-5.593	0.464	-0.189
Pure Al (99.99%)	2.0	-1.013	-4.902	0.324	-0.200
	6.5	-1.247	-5.932	0.492	-0.153
	9.0	-1.422	-5.467	1.424	-0.086

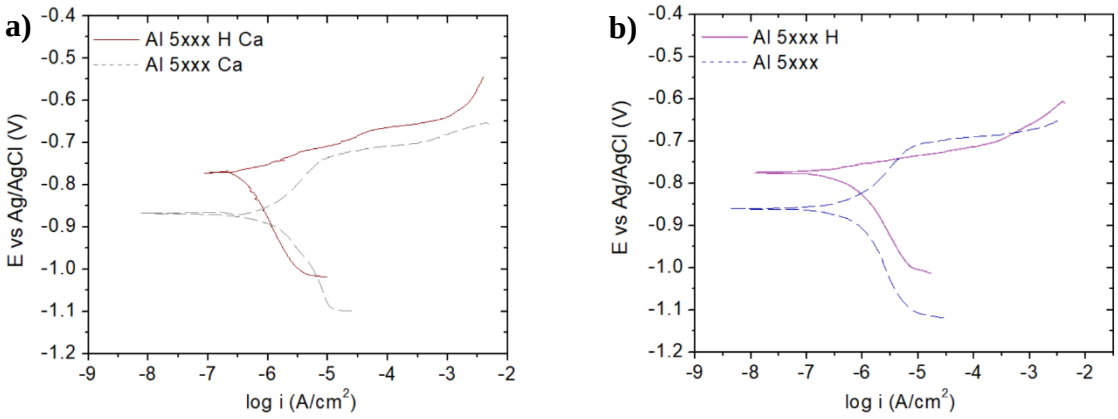

Figure 3.4: Comparisons of Tafel polarization of **a)** 5xxx H and **b)** 5xxx as-cast samples with and without Ca in 0.6 M NaCl at pH 6.5.

The overall corrosion potential (E_{corr}) in 5xxx Al alloys remains consistent as seen in Figure 3.9 below. 5xxx as-cast with and without Ca shows increased corrosion resistance owing to a lower corrosion current however the changes in current are minimal. The corrosion rate did not get altered significantly with the addition of Ca. Furthermore, the breakdown potential (E_{pit}) remains unchanged despite the addition of Ca or homogenization heat treatment. However, the degree of passivity in the homogenized alloy was seen to be influenced by the homogenization process (Figure 3.4). In 5xxx as-cast alloy, the OCP of 5xxx+Ca H is higher leading to greater corrosion potential and wider passivity range.

During the corrosion process, the presence of Mg which has higher affinity towards oxygen (Equation 25, 26 and 27) can form oxides in aqueous solution.

$$Mg \rightarrow Mg^{2+} + 2e^{-} \tag{25}$$

$$2H_2O + O_{2(aq)} + 4e^{-} \rightarrow 4OH^{-} \tag{26}$$

$$Mg + 2H_2O \rightarrow Mg(OH)_2 + H_2 \tag{27}$$

However, the $Mg(OH)_2$ cannot contribute towards the oxide layer as it can only be stable under strong alkaline conditions. This phase is then dissolved and OH^- dissociates into the electrolyte. This may increase the solution pH, but not enough to alter the pH_{pzc} of the alloy [24]. Here, the role of intermetallics is significant in the passivation and the corrosion behavior of the alloy.

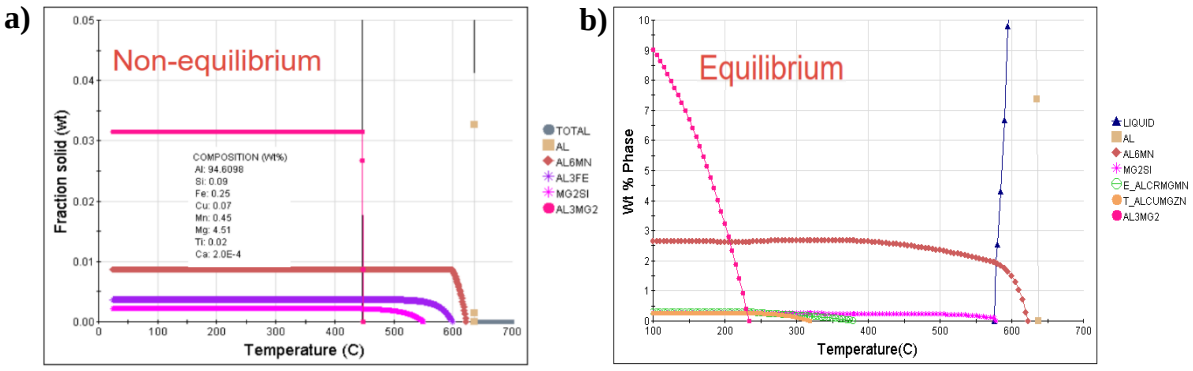

Figure 3.5: Thermodynamic calculations of phase fraction in alloy **a)** 5xxx assuming non-equilibrium solidification **b)** 5xxx assuming equilibrium solidification [25].

After the homogenization heat treatment, the thermodynamic calculations (Figure 3.5) of 5xxx Al alloy [25] shows lower percentage of Fe intermetallic phases, presence of Mg_2Si and increase in Al_3Mg_2 (β-phase). The Si phase is cathodic to the Al matrix, while the Mg_2Si phase is anodic to the Al matrix. Due to higher Mg to Si ratio in 5xxx Al alloy, usually the Mg_2Si is distributed discontinuously along the grain boundaries [26]. During the corrosion process, the Mg dissolves from the Mg_2Si particle and enriches the presence of Si. This Si enrichment leads the Mg-depleted Mg_2Si particle to act as a cathode and move the particle potential to a more positive direction resulting in corrosion of Al matrix. The schematic of Mg_2Si dissolution and its contribution to corrosion process is described through the schematic in Figure 3.7. However, contribution of Mg_2Si in corrosion is said to be less prominent due to the active dissolution of Mg. There are also reports that suggest the presence of Si and β-phase at the grain boundary of 5xxx after homogenization [19,26,27]. As the 5xxx Al alloy is exposed to the corrosive environment, highly anodic precipitates such as β-phase start to react. Increased precipitation with homogenization of anodic intermetallic like β-phase will not only introduce micro-galvanic corrosion but also disrupt the oxide layer acting as sites for corrosion. The sudden increase in the corrosion current in the homogenized 5xxx Figure 3.4 (a and b) corresponds to the increase in the intermetallic ratio compared to the as-cast alloy. The reduced number of precipitates in the as-cast samples contributes towards the corrosion resistance through reduced microgalvanic corrosion and less disruption in the oxide layer owing to a slightly improved passivity as seen in Figure 3.4.

3.1.2 Effect of pH using Tafel Polarization on 6xxx Al Alloys

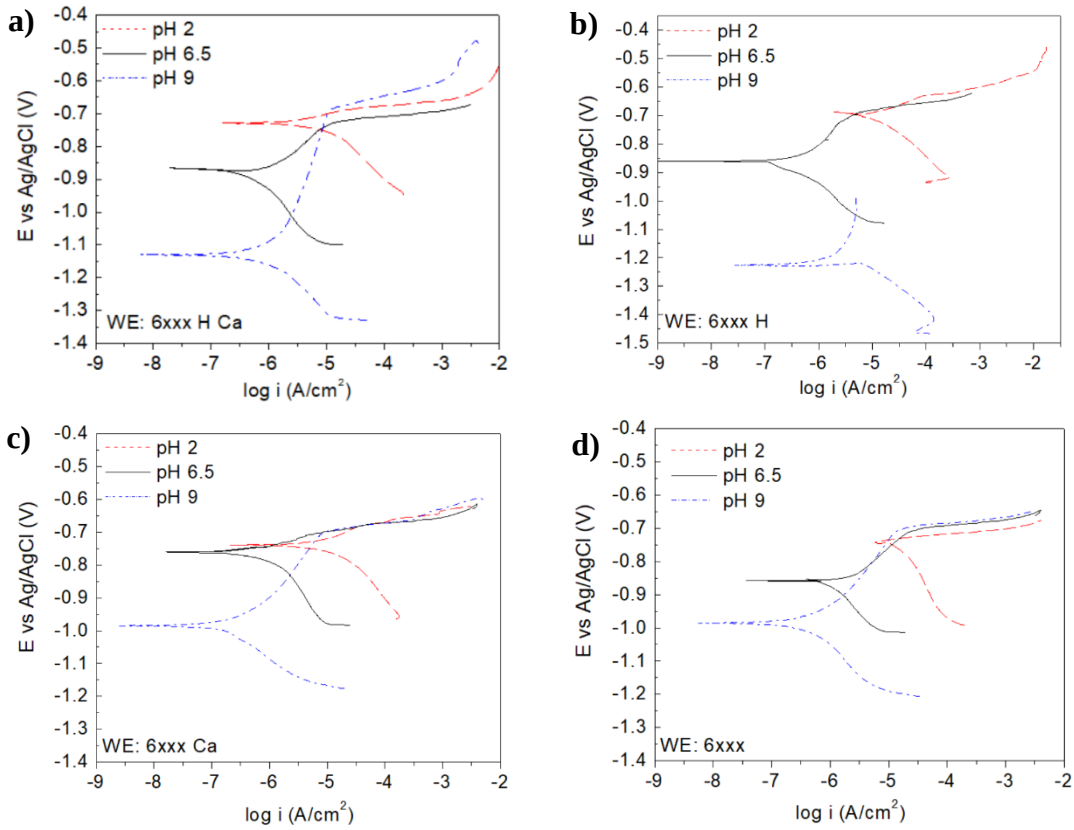

Figure 3.6: Effect of pH on the Tafel polarization of **a)** 6xxx HOMO Ca **b)** 6xxx HOMO **c)** 6xxx as-cast with Ca **d)** 6xxx as-cast.

The corrosion rates (i_{corr}) in 6xxx Al alloys are comparable between to as cast and homogenized samples, based on the similar E_{corr} and i_{corr} values in Figure 3.6 and 3.10. Zeng et. al. [17] identified alloys with Mg to Si ratio greater than 1.73 may be susceptible to IGC however alloys with ratios less than 1.73 (6xxx with Mg to Si ratio of 0.8) showed Mg_2Si and Si precipitates near the grain boundary. The dissolution of Mg_2Si can further be described through the following equations:

$$Mg_2Si + 4H_2O \rightarrow 2Mg(OH)_2 + SiH_4 \quad (28)$$

$$SiH_4 + mH_2O \rightarrow SiO_2.nH_2O + 4H_2\uparrow \quad (29)$$

$$Mg_2Si + 2H_2O \rightarrow 2Mg^{2+} + SiO_2 + 4H^+ + 8e^- \quad (30)$$

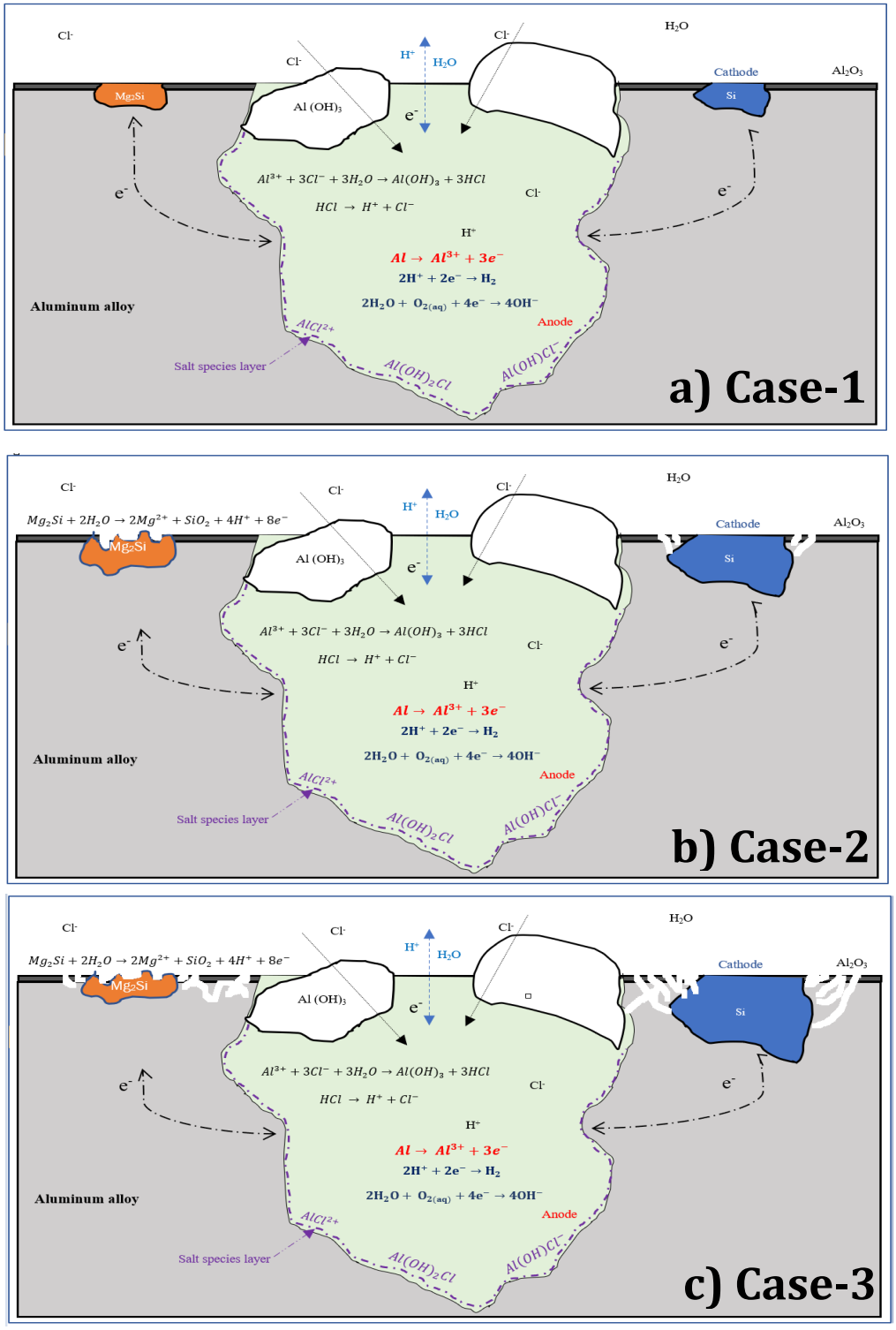

Figure 3.7: Schematic mechanism of function mechanism of Mg_2Si and Si precipitates in localized corrosion of Al-Mg-Si alloys. **a)** Mg_2Si and Si particles on the Al surface **b)** Corrosion initiates on the Mg_2Si surface and near the periphery free zones (PFZ) near the Si particle. **c)** Corrosion of PFZ at periphery of Mg_2Si and Si particles [17].

Initially, the Mg_2Si is hydrolyzed (Equation 28) releasing SiH_4 and its subsequent hydrolysis (Equation 29), releases hydrogen and silicon hydroxides near the Mg_2Si intermetallic. This electrochemical dissolution can enrich the Si (Equation 30) during the anodic dissolution of Mg_2Si. Initially Mg_2Si and Si are present on the surface, anodic dissolution leads to the preferential dissolution of Mg and enrichment of Si (Figure 3.7b). This causes the electrochemical activity of anodic Mg_2Si to be cathodic to bulk Al. As corrosion continues (Figure 3.7c)., enriched Si particles are cathodic to the matrix and leads to further anodic dissolution near the precipitate free zones (PFZ) near Mg_2Si and Si particles.

The homogenization heat treatment in as-cast 6xxx without Ca has affected the Mg_2Si content as seen from the thermodynamic calculations in Fig 23 below, but the corrosion resistance seems to remain unaffected. With changes in the calcium content, the level of passivity is altered in the Al 6xxx alloy with Ca (Figure 3.8). The passivation in the Al 6xxx alloy without Ca does not seem to be influenced unlike the 5xxx Al alloys.

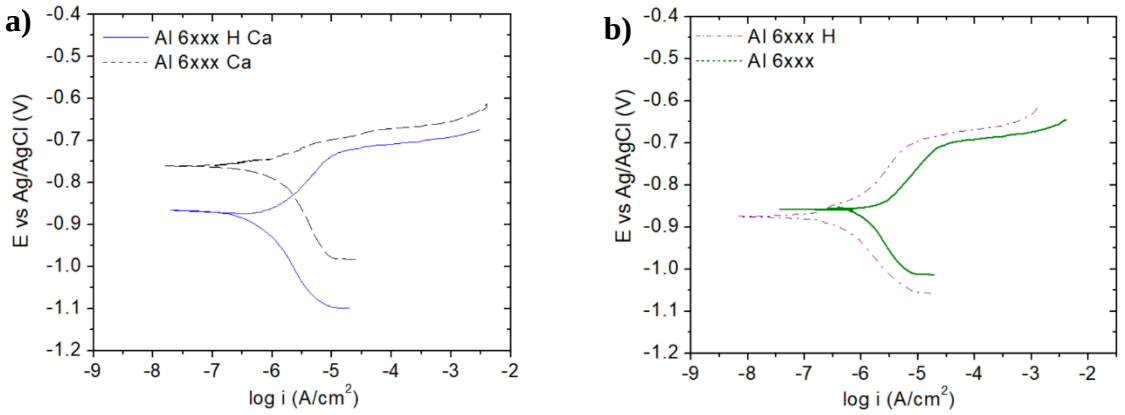

Figure 3.8: Comparisons of Tafel polarization of **a)** 6xxx H and **b)** 6xxx as-cast samples with and without Ca in 0.6 M NaCl at pH 6.5.

Microstructural analysis through polarized imaging (Figure. 3.39) in the following section showed added Ca to increase the intermetallic size of as-cast 6xxx Al alloy. This increase in the intermetallic area can influence the corrosion properties as discussed in the previous sections. Presence of larger cathodic intermetallic such as Si after the dissolution of Mg_2Si, can influence the corrosion of the Al 6xxx alloy [5,18].

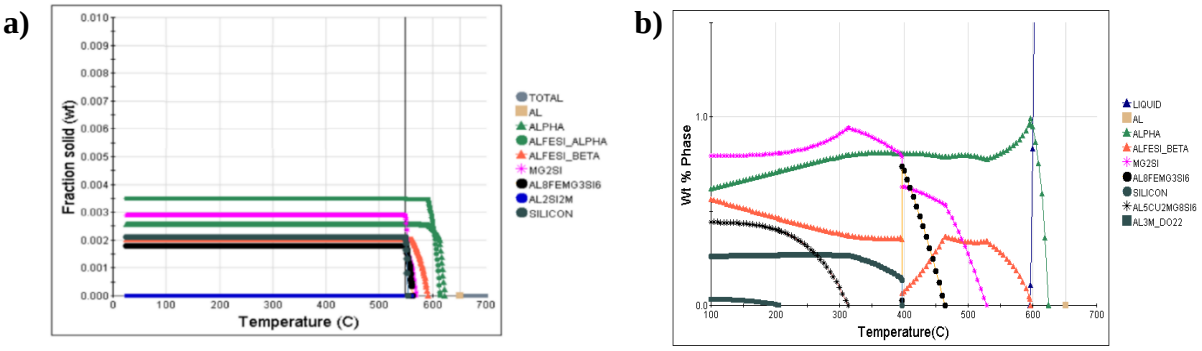

Figure 3.9: Thermodynamic calculations of phase fraction in alloy **a)** 6xxx assuming non-equilibrium solidification **b)** 6xxx assuming equilibrium solidification [25].

Table 3.2: Summary of Tafel data of 6xxx aluminum alloys in 0.6 M NaCl at pH 6.5 solution.

Alloy	pH	E_{corr} (V)	I_{corr} (A/cm^2)	βa (V/decade)	βc (V/decade)
6xxx+Ca H	2.0	-0.701	-5.186	0.014	-0.169
	6.5	-0.905	-6.153	0.229	-0.268
	9.0	-1.151	-5.845	0.506	-0.167
6xxx H	2.0	-0.677	-5.032	0.034	-0.154
	6.5	-0.887	-6.351	0.188	-0.145
	9.0	-1.179	-5.384	0.431	0.132
6xxx+Ca	2.0	-0.708	-4.949	0.038	-0.194
	6.5	-0.777	-6.187	0.081	-0.227
	9.0	-1.028	-6.481	0.235	-0.127
6xxx	2.0	-0.728	-4.750	0.015	-0.383
	6.5	-0.886	-5.813	0.158	-0.215
	9.0	-1.005	-6.220	0.214	-0.197

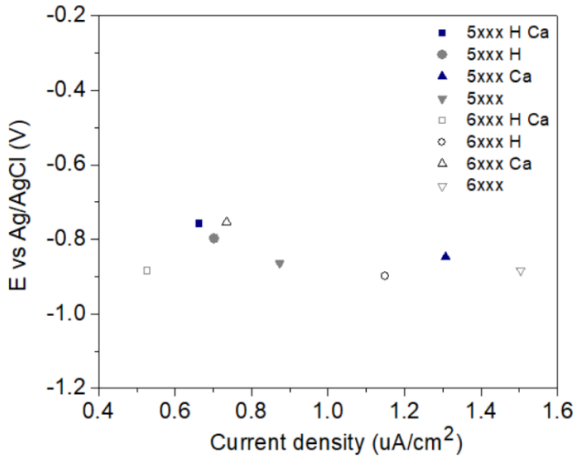

Figure 3.10: Comparison of Tafel data (Ecorr vs icorr) between 5xxx and 6xxx in 0.6M NaCl at pH 6.5.

3.1.3. Effect of pH using Tafel Polarization on Rolled Alloys

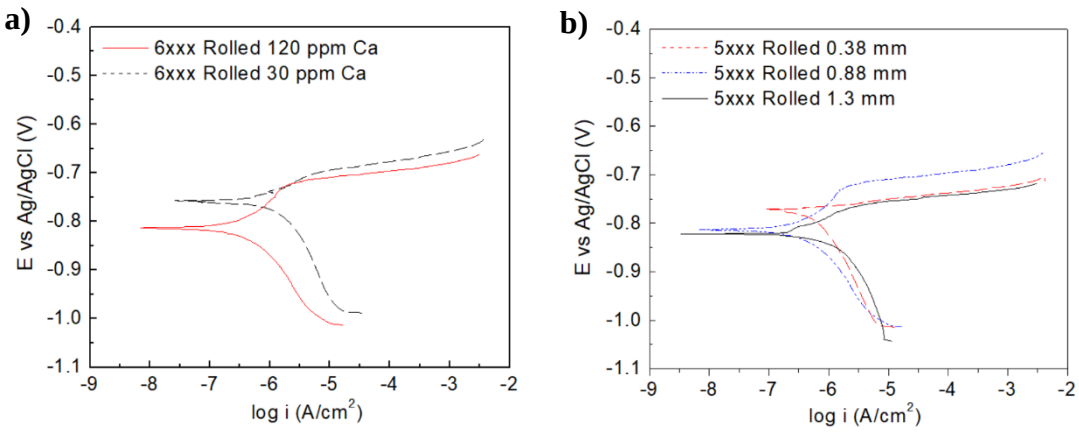

Figure 3.11: Tafel polarization of **a)** Rolled 6xxx **b)** Rolled 5xxx with 0.6 M NaCl at pH 6.5.

Table 3.3: Summary of Tafel data of rolled alloys in 0.6 M NaCl at pH 6.5 solution.

Alloy	pH	E_{corr} (V)	I_{corr} (A/cm^2)	βa (V/decade)	βc (V/decade)
Rolled 6xxx 30 ppm Ca	6.5	-0.729	-5.777	0.057	-0.303
Rolled 6xxx 120 ppm Ca		-0.800	-6.304	0.134	-0.198
Rolled 5xxx 0.38 mm	6.5	-0.769	-6.200	0.017	-0.228
Rolled 5xxx 0.88 mm		-0.793	-6.298	0.125	-0.200
Rolled 5xxx 1.3 mm		-0.774	-5.742	0.060	-0.372

The corrosion behavior of rolled 6xxx sheet was studied with varying concentration of calcium. As it can be seen from Figure 3.11a and Table 3.2, the corrosion potential decreases as the calcium content in the alloy is increased. The corrosion current was also seen to shift slightly in the negative direction for the 6xxx rolled Al alloys with 120 ppm Ca. However, these changes in corrosion resistance are very minor and more studies should be done with higher concentrations of Ca.

In the rolled 5xxx Al alloy, the effect of varying sheet thickness on the corrosion behavior was studied. Despite changes in the microstructure and sheet thickness, there was minimal changes in the corrosion behavior from Figure 3.11b and Table 3.2. The changes in microstructure and fabrication process did not seem to affect the overall electrochemical behavior however the microstructural damage due to corrosion must be investigated further.

3.1.4 Effect of pH using Cyclic Polarization on 5xxx Al Alloys

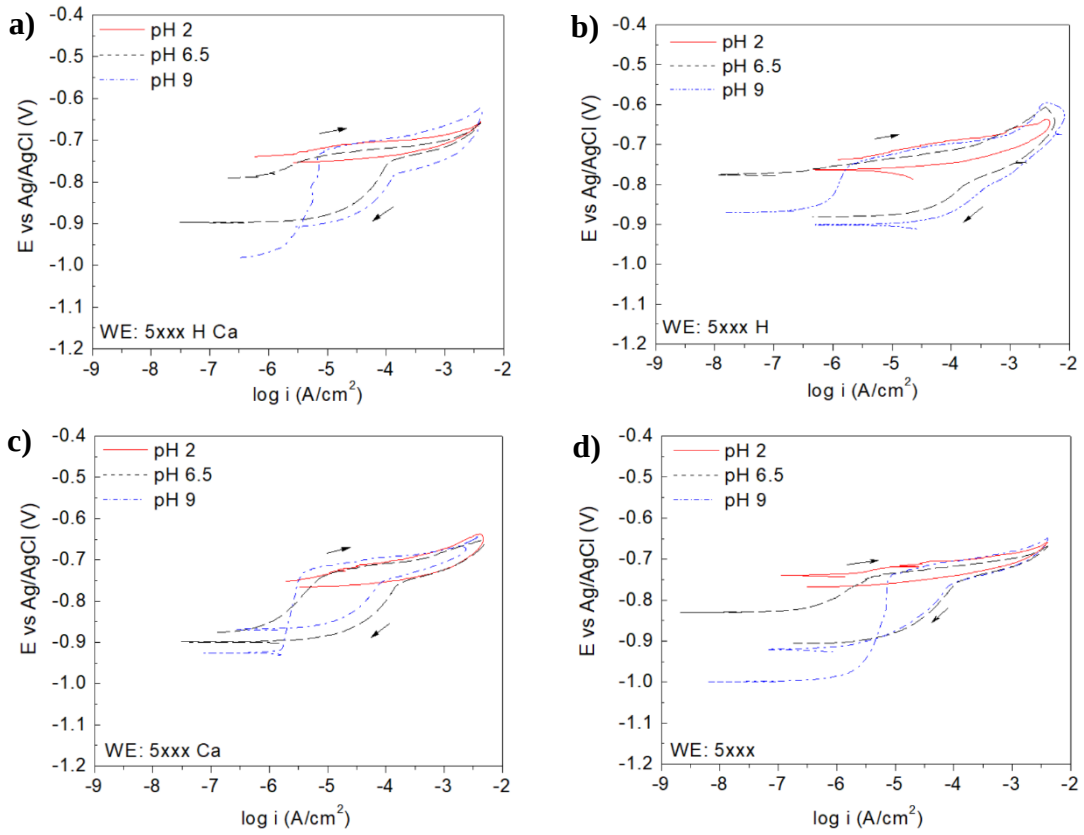

Figure 3.12: Effect of pH on the cyclic polarization of **a)** 5xxx H Ca **b)** 5xxx H **c)** 5xxx Ca **d)** 5xxx.

The effect of pH on the repassivation response of 5xxx Al alloys is demonstrated in Figure 3.12. Regardless of alloy composition and homogenization process, the repassivation potential (E_{ptp}) is not seen for low pH 2. No initial passivity in the forward scan and immediate repassivation is seen at low pH due to the high solubility of Al^{3+} in the acidic solution. Furthermore, E_{ptp} and E_{prot} vary minimally as pH is increased to pH 6.5 and 9 suggesting a similar repassivation response. E_{ptp} is seen to be pH independent and the size of the hysteresis $|E_{pit} - E_{ptp}|$ remains consistent throughout pH changes within the alloys.

3.1.5 Effect of pH using Cyclic Polarization on 6xxx Al Alloys

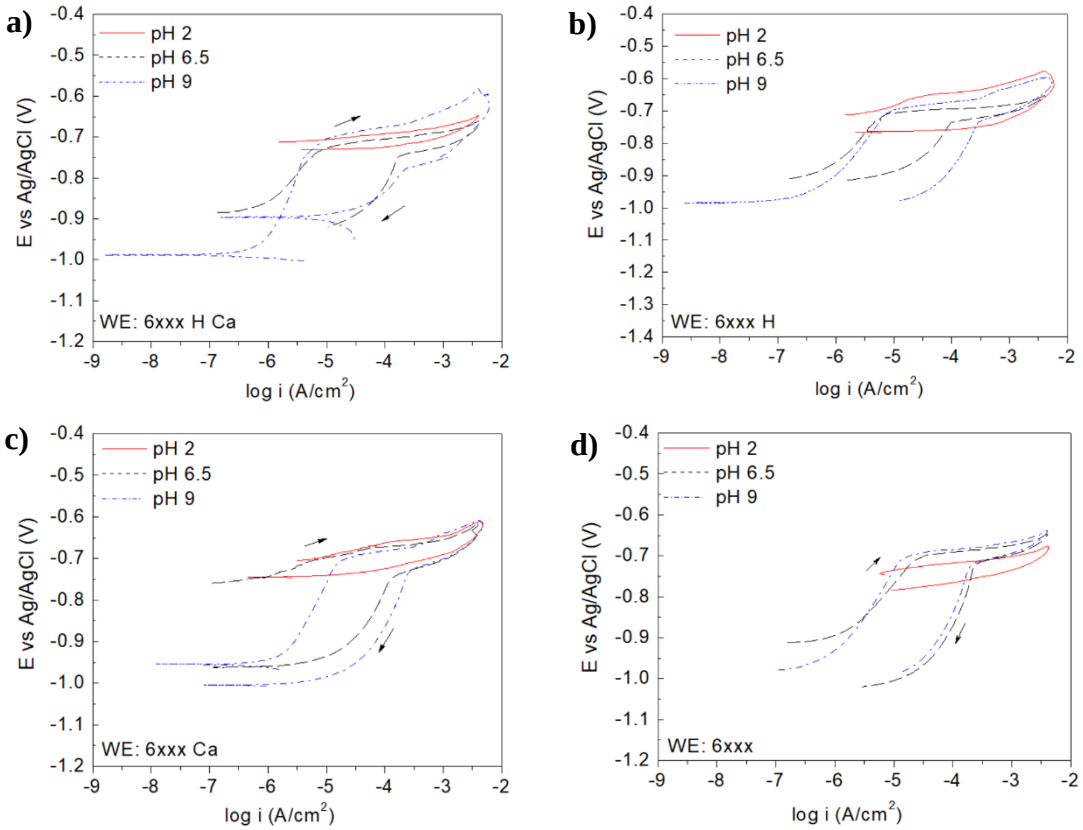

Figure 3.13: Effect of pH on the cyclic polarization of **a)** 6xxx H Ca **b)** 6xxx H **c)** 6xxx Ca **d)** 6xxx.

The breakdown potential (E_{pit}) in the forward scan of cyclic polarization (Figure 3.14) shows only small variations with changes in Ca content. E_{pit} is seen to be consistent despite changes in alloy fabrication. In addition, characteristic electrochemical behavior in the reverse scan E_{ptp} and i_{ptp} are not influenced by the addition of calcium suggesting similar repassivation behavior.

As-cast samples in the case of 6xxx with and without Ca show a steeper response during the reverse curve owing to a wider hysteresis. The wider hysteresis or the $\Delta E = E_{pit} - E_{prot}$ in the as-cast 6xxx alloys show increased susceptibility to localized corrosion as seen in Table 3.4.

3.1.6 Effect of Concentration on 5xxx Al Alloys

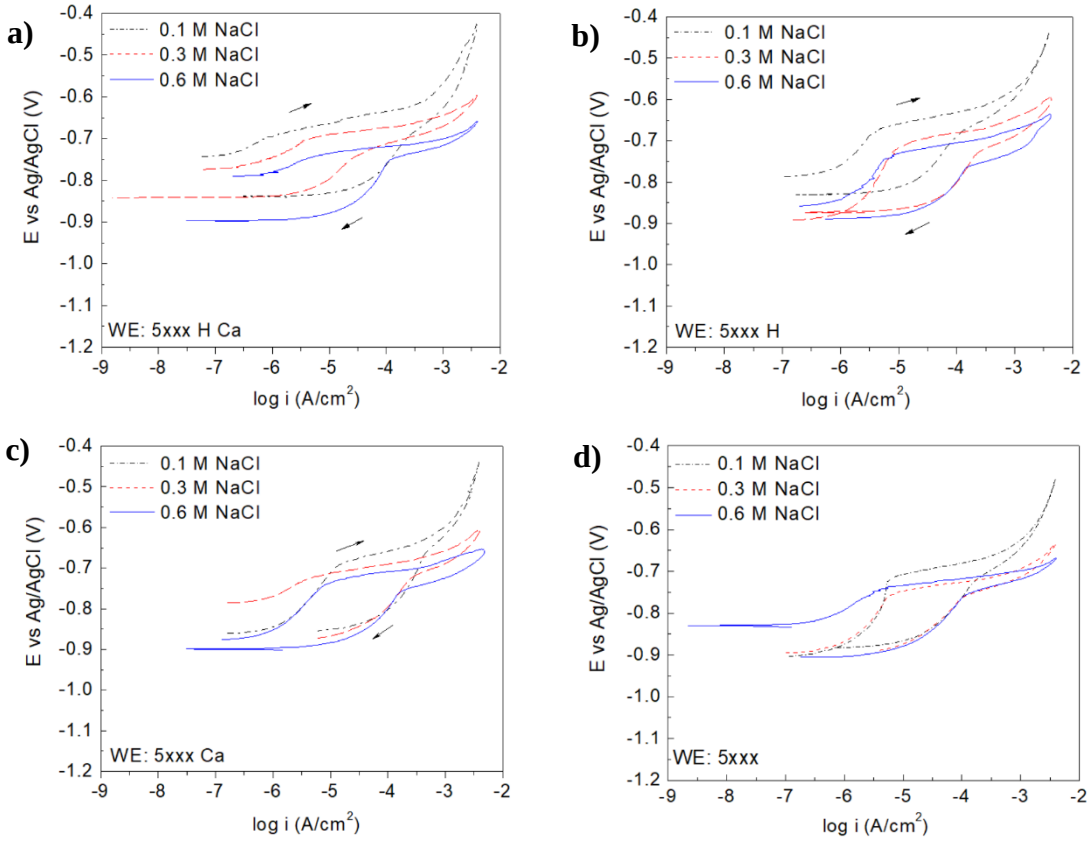

Figure 3.14: Effect of concentration on the cyclic polarization of **a)** 5xxx H Ca **b)** 5xxx H **c)** 5xxx Ca **d)** 5xxx.

The characteristic electrochemical parameters calculated from the cyclic polarization of 5xxx alloys at varying concentrations are reported in Table 3.3 and Figure 3.14. The varying concentration of Cl^- shows a trend of decreasing E_{ptp}. The increase in Cl^- concentration showed an effect in the forward scan lowering the breakdown potential (E_{pit}) to more negative values. The critical pit concentration will be diluted with lower Cl^- concentration but repassivation is supported with the limited Cl^- concentration in the bulk. Epit ≃ Eptp at lower concentrations due to similar local activity while at higher concentrations, the difference in $|E_{pit} - E_{ptp}|$ increases indicating the increase in propagation of localized corrosion. Additionally, i_{ptp} is seen to occur at higher current compared to i_{pit}. Comotti et. al. [28] suggested that i_{ptp} is a function of the extent of promoted corrosion while E_{ptp} is independent of surface state condition and is a characteristic of the alloy in each corrosive environment. E_{pit} is seen to be differ minimally at higher concentrations however through additional studies below showed a linear decrease in the breakdown potential with rising Cl^- concentration.

Table 3.4: Summary of cyclic polarization data of 5xxx aluminum alloys with varying NaCl concentration at pH 6.5 solution.

Alloy	Concentration	Epit (V)	Eptp (V)	log(iptp) (A/cm^2)	Steepness
	0.1 M	-0.695	-0.688	-3.536	0.223
	0.3 M	-0.706	-0.733	-4.437	0.315
5xxx H Ca	0.6 M	-0.721	-0.758	-4.091	0.586
	0.1 M	-0.699	-0.693	-3.913	0.132
	0.3 M	-0.702	-0.734	-3.667	0.225
5xxx H	0.6 M	-0.744	-0.759	-4.001	0.375
	0.1 M	-0.69	-0.668	-3.296	0.231
	0.3 M	-0.721	-0.724	-3.651	0.197
5xxx Ca	0.6 M	-0.735	-0.756	-3.760	0.168
	0.1 M	-0.71	-0.724	-3.724	0.143
	0.3 M	-0.746	-0.76	-3.998	0.120
5xxx	0.6 M	-0.737	-0.764	-3.982	0.155

3.1.7 Effect of Concentration on 6xxx Al Alloys

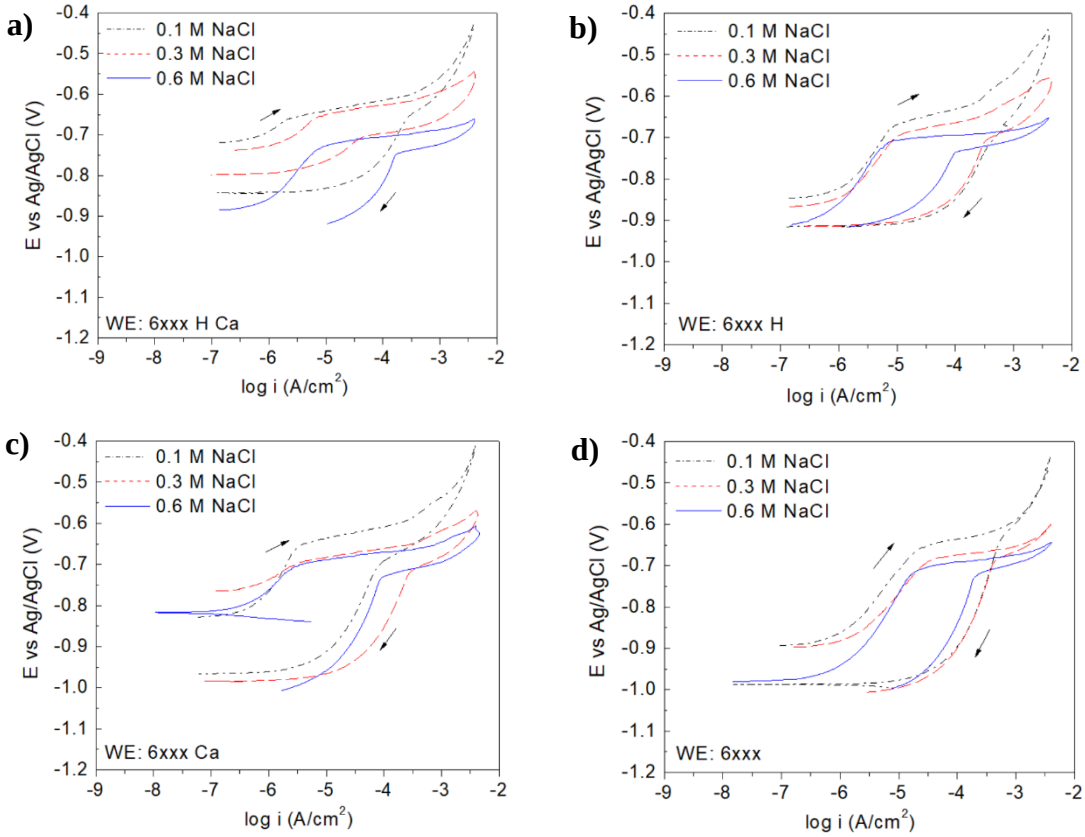

Figure 3.15: Effect of concentration on the cyclic polarization of **a)** 6xxx H Ca **b)** 6xxx H **c)** 6xxx Ca **d)** 6xxx.

The 6xxx Al alloys showed a similar response in terms of the effect of concentration, as discussed in the earlier section. From Figure 3.16, there are no contrasts in the characteristic electrochemical parameters between the homogenized alloys. However, the propensity of localized attack in 0.6 M NaCl, judged through the size of the hysteresis is $\Delta E = E_{pit} - E_{prot}$ in as-cast alloys are greater compared to the homogenized alloys (illustrated in Figure 3.17b).

Table 3.5: Summary of cyclic polarization data of 6xxx aluminum alloys with varying NaCl concentration at pH 6.5 solution.

Alloy	Concentration	Epit (V)	Eptp (V)	log(iptp) (A/cm^2)	Steepness
	0.1 M	-0.66	-0.65	-3.530	0.238
	0.3 M	-0.66	-0.704	-4.289	0.095
6xxx H Ca	0.6 M	-0.7216	-0.746	-3.749	0.321
	0.1 M	-0.671	-0.692	-3.265	0.223
	0.3 M	-0.689	-0.709	-3.469	0.315
6xxx H	0.6 M	-0.702	-0.736	-4.019	0.289
	0.1 M	-0.665	-0.685	-4.047	0.307
	0.3 M	-0.684	-0.719	-3.524	0.295
6xxx Ca	0.6 M	-0.694	-0.732	-3.923	0.227
	0.1 M	-0.655	-0.634	-3.25	0.405
	0.3 M	-0.687	-0.687	-3.362	0.3042
6xxx	0.6 M	-0.709	-0.731	-3.75	0.4792

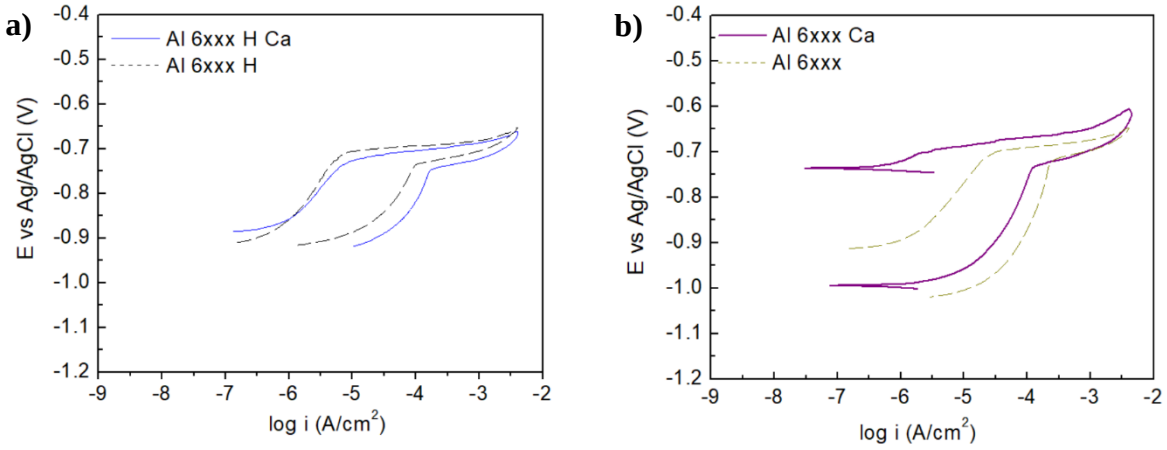

Figure 3.16: Comparison between the cyclic polarization of **a)** homogenized 6xxx alloys **b)** as- cast 6xxx alloys at 0.6 M NaCl at pH 6.5.

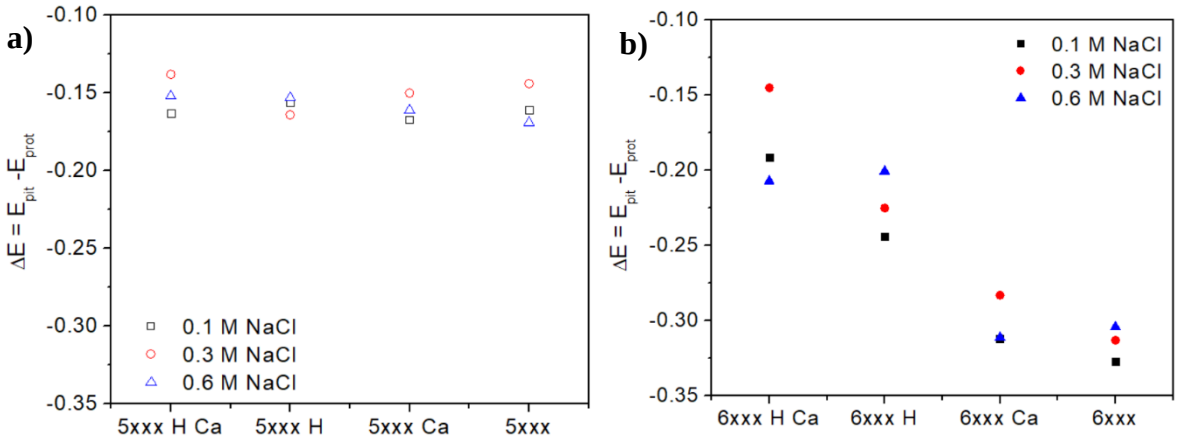

Figure 3.17: Comparisons on the hysteresis ($\Delta E = E_{pit} - E_{prot}$) from the cyclic polarization of **a)** 5xxx and **b)** 6xxx alloys with increasing chloride concentration.

With the increasing Cl^- concentration, the extent of localized corrosion indicated through the size of the hysteresis ($\Delta E = E_{pit} - E_{prot}$) in Figure 3.17 varies with increasing concentration. The protection potential E_{prot} increases with lower Cl^- concentrations in both alloys. The extent of Cl^- concentration affects the initiation of the pits (E_{pit}) and the transition onset during repassivation (E_{ptp}). The critical pit chemistry is concentrated, however the repassivation through dilution of the occluded pit is limited even though the external Cl^- concentration decreases. The transition potential E_{ptp} is indicative of the competitive repassivation and active corrosion during the repassivation process. The mass transfer between the pit and the bulk is limited and can occur even after complete repassivation of the pit cavity surface [12]. The hysteresis ($\Delta E = E_{pit} - E_{prot}$) remained consistent for the 5xxx Al alloys at all concentrations. In the 6xxx Al alloys, homogenized alloys with calcium showed least propensity towards localized attack however, as-cast alloys showed increased propensity towards localized corrosion as seen in Figure 3.16b and Figure 3.17b. The microstructural damage due to localized corrosion between homogenized and as-cast samples are compared and discussed in the next section.

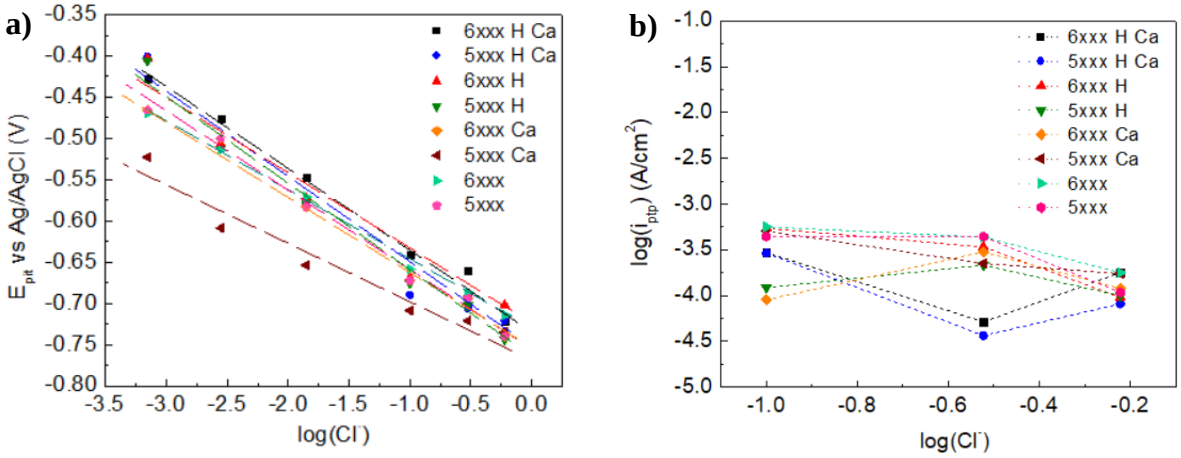

Figure 3.18: a) Variation of E_{pit} with increasing chloride concentration **b)** Variation in i_{ptp} with increase in chloride

The result illustrated in Figure 3.18a shows the linear dependance of the breakdown potential (E_{pit}) as a function of chloride ion activity. The anodic polarization of the 5xxx and 6xxx alloys showing the decreasing Epit vs log (Cl^-) is provided in Appendix. At low concentrations, supporting electrolyte 0.1 M $NaClO_4$ was added to increase the conductivity of the solution. The concentration of Cl^- was varied from 0.1 M NaCl to lower concentrations to see the changes in the breakdown potential. At 25 ppm Cl^-, the breakdown potential did not change from the chloride free solution. This is true in the case of 6xxx and 5xxx alloys, which showed similar thresholds despite changes in composition and homogenization. The linear decrease in the breakdown potential showed similar slope response amongst the 5xxx and 6xxx Al alloys which can be explained through the modification of the Nernst relation in Equation 1:

$$E = E_o - \frac{2.303RT}{nF}\log(Cl^-) \tag{31}$$

The relationship between $\log(i_{ptp})$ and log Cl^- concentration in Figure 3.18b allows for the estimation of the order of reaction with respect to chloride ion concentration. The slopes (n) close to 0, indicates the rate of equilibrium hydrolysis at E_{ptp} does not depend on the Cl^- concentration and chloride is catalytic during the repassivation process. However, the fractional values of n indicate a more complex reaction mechanism during repassivation [12].

3.1.8 Effect of Cyclic Polarization of 5xxx Al Alloys under Controlled Atmosphere

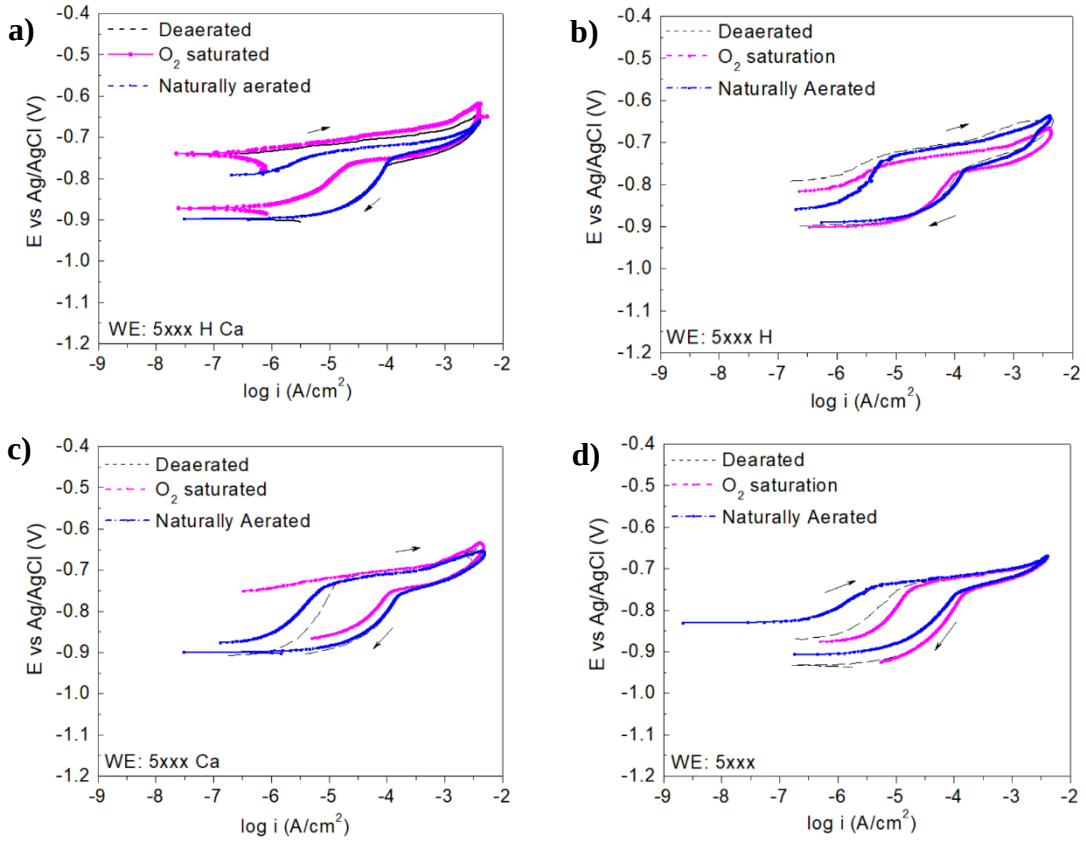

Figure 3.19: Cyclic polarization response of 5xxx alloys under controlled atmosphere in 0.6 M NaCl at pH 6.5.

The effects of controlled atmosphere under deaerated, naturally aerated and O_2 saturated conditions in 0.6 M NaCl at pH 6.5 were studied using cyclic polarization as seen in Figure 3.19. Despite changes in cell conditions in the 5xxx alloys, the overall behavior of the alloys remain the same. The breakdown potentials and the reverse re-passivation potentials are coherent in all three conditions with minor changes. Oxygen dissolved in the solution also is seen to have less influence on the localized behavior of the alloy. However, increase in dissolved oxygen content reduced the passivity level in the 5xxx Al alloys with Ca. In the case of deaerated condition, the cyclic polarization graphs between the alloys were overlapped and a significant difference in corrosion behavior could not be observed.

3.1.9 Effect of Cyclic Polarization of 6xxx Al Alloys under Controlled Atmosphere

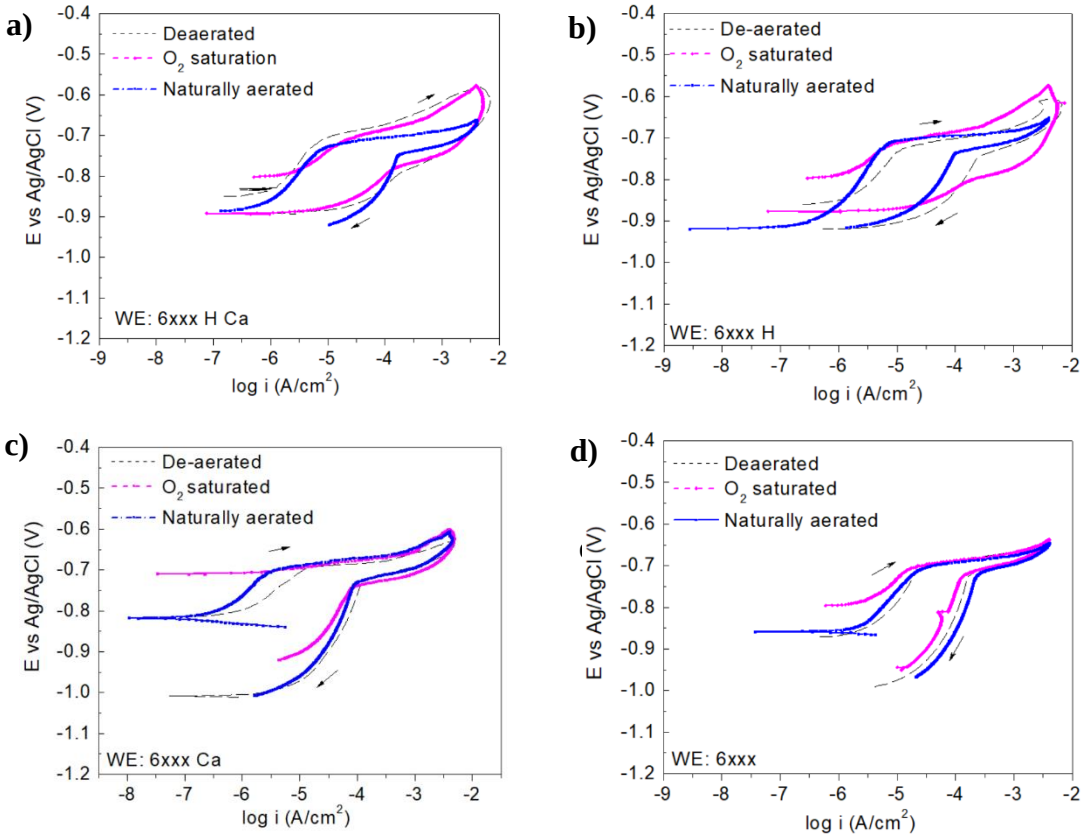

Figure 3.20: Cyclic polarization response of 6xxx alloys under controlled atmosphere in 0.6 M NaCl at pH 6.5.

During the O_2 saturation process, the anodic corrosion process was seen to alter passivity of 6xxx Ca in Figure 3.20c. However, in cases with the other 6xxx Al alloys, this variation in the forward scan cannot be seen. Despite these changes, the characteristic potentials remain fixed in all cases provided a few changes. This leads to the conclusion that under de-aerated and naturally aerated condition, the anodic behavior of the alloys is minimally affected however the initial passivity is affected in the O_2 saturated condition.

Table 3.6: Summary of cyclic polarization data of 5xxx aluminum alloys under controlled atmosphere in 0.6 M NaCl pH 6.5 solution.

Alloy	Condition	E_{pit} (V)	E_{ptp} (V)	Log(I_{ptp}) (A/cm^2)
	Naturally Aerated	-0.72	-0.76	-4.09
	De-aerated	-0.71	-0.77	-3.98
5xxx H Ca	Oxygen Saturated	0.72	-0.77	-4.59
	Naturally Aerated	-0.74	-0.76	-4.00
	De-aerated	-0.73	-0.77	-3.84
5xxx H	Oxygen Saturated	-0.74	-0.76	-3.39
	Naturally Aerated	-0.74	-0.75	-3.73
	De-aerated	-0.73	-0.76	-3.80
5xxx Ca	Oxygen Saturated	-0.72	-0.75	-3.97
	Naturally Aerated	-0.74	-0.73	-3.97
	De-aerated	-0.75	-0.76	-0.82
5xxx	Oxygen Saturated	-0.75	-0.76	-3.84

Table 3.7: Summary of cyclic polarization data of 6xxx aluminum alloys under controlled atmosphere in 0.6 M NaCl pH 6.5 solution.

Alloy	Condition	E_{pit} (V)	E_{ptp} (V)	log (I_{ptp}) (A/cm^2)
	Naturally Aerated	-0.72	-0.75	-3.75
	De-aerated	-0.72	-0.77	-3.78
6xxx H Ca	Oxygen Saturated	-0.78	-0.74	-3.80
	Naturally Aerated	-0.70	-0.74	-4.02
	De-aerated	-0.73	-0.75	-3.62
6xxx H	Oxygen Saturated	-0.72	-0.81	-3.74
	Naturally Aerated	-0.70	-0.73	-3.96
	De-aerated	-0.70	-0.74	-3.89
6xxx Ca	Oxygen Saturated	-0.70	-0.74	-4.13
	Naturally Aerated	-0.71	-0.72	-3.75
	De-aerated	-0.71	-0.72	-3.76
6xxx	Oxygen Saturated	-0.71	-0.72	-3.89

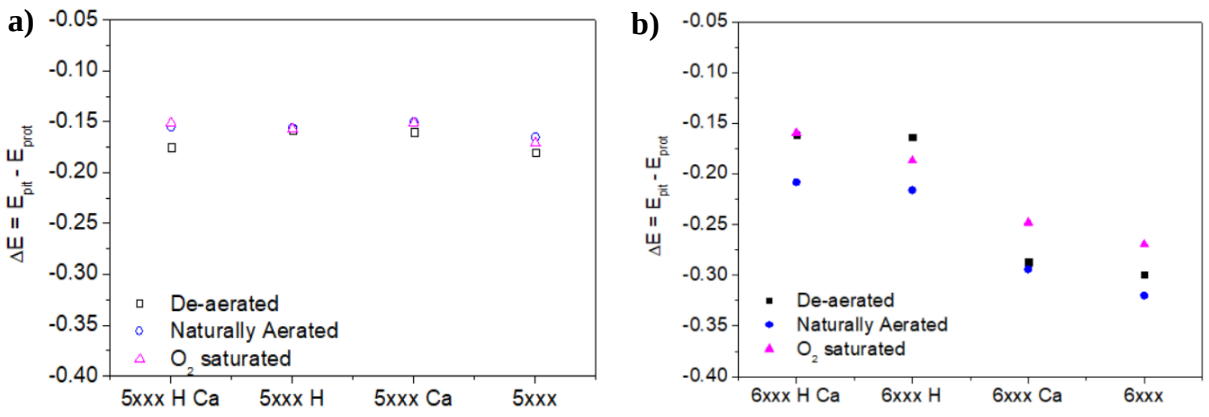

Figure 3.21: Comparisons on the hysteresis ($\Delta E = E_{pit} - E_{prot}$) from the cyclic polarization of **a)** 5xxx and **b)** 6xxx alloys under controlled atmosphere.

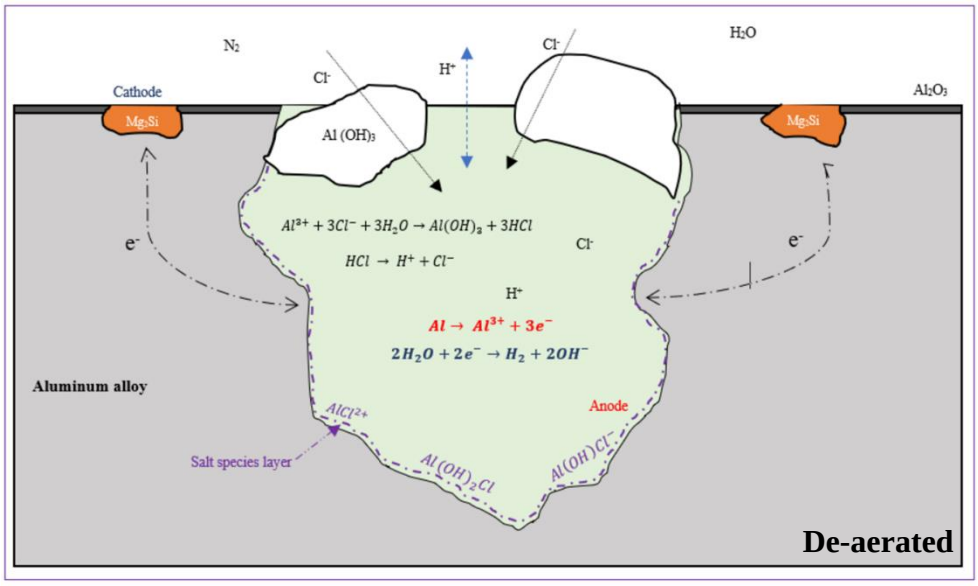

Figure 3.22: Schematic of pitting corrosion under de-aerated condition.

The extent of localized corrosion ($\Delta E = E_{pit} - E_{prot}$) in Figure 3.21a showed little effect in the 5xxx alloys despite changes in the cell conditions. Under de-aerated conditions, the absence of O_2 in the cell, limits the cathodic half-cell reaction in Equation 14. However, the dissociation of salt layer and presence of additional Cl^- can introduce HCl as seen in Equation 20. H^+ evolution within the pit can support the cathodic reaction in Equation 32.

$$2H_2O + O_{2(aq)} + 4e^- \rightarrow 4OH^- \quad (14)$$

$$2H^+ + 2e^- \rightarrow H_2 \quad (15)$$

$$Al^{3+} + 3Cl^- + 3H_2O \rightarrow Al(OH)_3 + 3HCl \quad (20)$$

$$2H_2O + 2e^- \rightarrow H_2 + 2OH^- \quad (32)$$

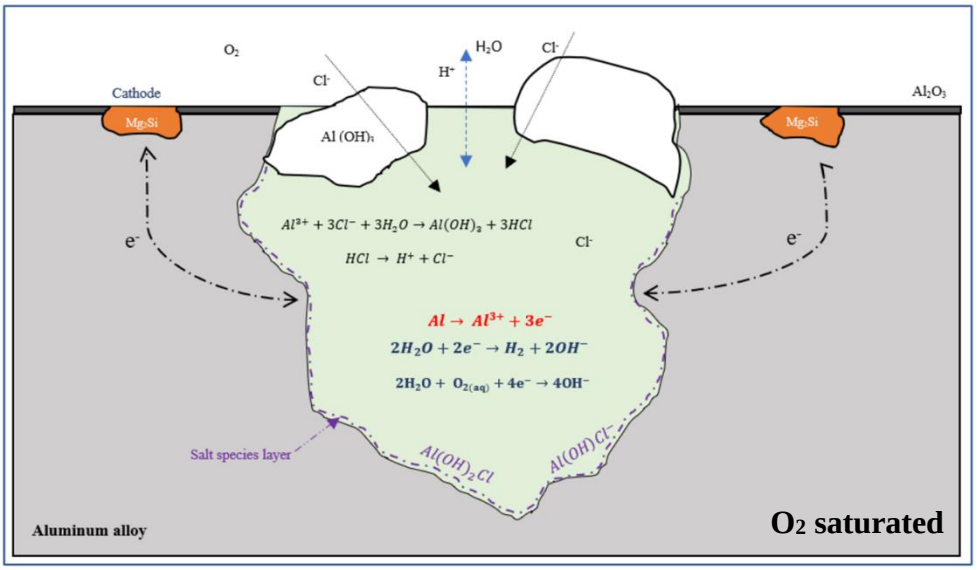

Figure 3.23: Schematic of pitting corrosion under O_2 saturated condition.

The increase in O_2 content in the aqueous solution, can influence the cathodic reaction in Equation 14. Increase in the cathodic reaction rate, must influence the half-cell reaction, and further increase the anodic half-cell reaction with anodic dissolution. The rate of corrosion during the O_2 saturated condition is much higher in the 5xxx Al alloys with Ca. Trace amount of Ca is shown to influence the microstructure of the alloy in Figure 3.39 in the following section. These changes much be considered as, the dissolution of the metal can occur adjacent to the weak oxide film near the intermetallic. Perhaps, Ca involvement in the 5xxx microstructure could have influenced the size and distribution of

intermetallic like Mg_2Si. This requires further investigation. In the case of 6xxx Al alloy, the increase in the localized corrosion is related to the pitting mechanism explained in the following section.

3.1.10 Effect of Sensitization on 5xxx Al Alloys

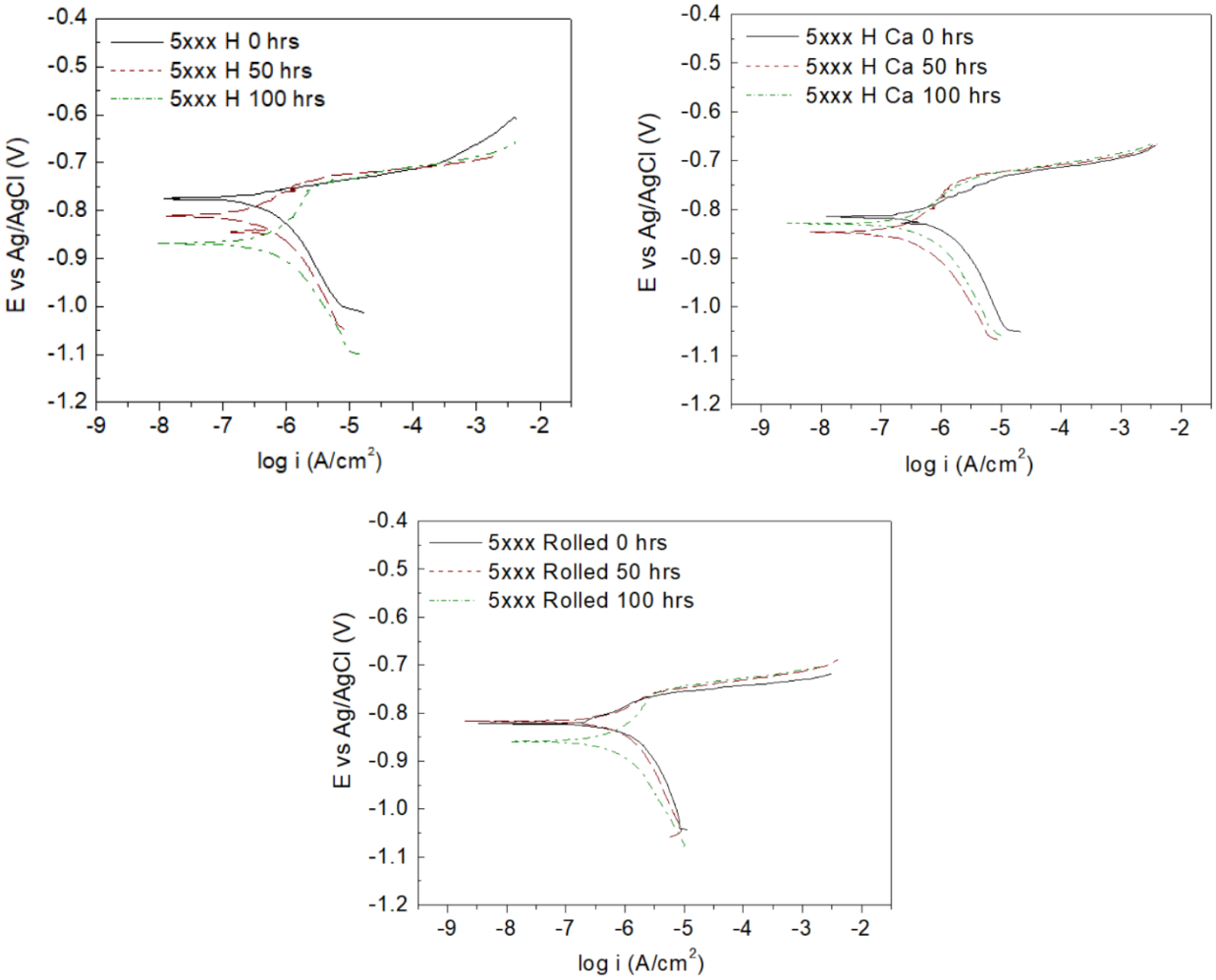

Figure 3.24: Effect of sensitization time on the Tafel polarization of alloys **a)** 5xxx H, **b)** 5xxx H Ca, and **c)** rolled 5xxx in 0.6 M NaCl at pH 6.5. 5xxx alloy solution heat treated (SHT) at 450°C for 1 hr. and heat treated at 150°C for 0 hrs., 50 hrs., and 100 hrs.

Table 3.8: Summary of Tafel polarization results as a function of sensitization of alloys in 0.6 M NaCl at pH 6.5.

Alloy	**Sensitization Time**	**E_{corr} (V)**	**log(I_{corr}) (A/cm^2)**	**βa (V/decade)**	**βc (V/decade)**
5xxx H	0 hrs.	-0.780	-5.94	0.019	-0.240
	50 hrs.	-0.815	-6.33	0.085	-0.278
	100 hrs.	-0.840	-6.07	0.194	-0.242
5xxx+Ca H	0 hrs.	-0.780	-5.94	0.045	-0.255
	50 hrs.	-0.809	-6.26	0.066	-0.311
	100 hrs.	-0.798	-6.22	0.071	-0.255
Rolled 5xxx+Ca	0 hrs.	-0.776	-5.83	0.052	-0.309
	50 hrs.	-0.782	-5.93	0.059	-0.403
	100 hrs.	-0.846	-6.06	0.008	-0.450

The effect of sensitization time onto the corrosion behavior of 5xxx H, 5xxx+Ca H and rolled 5xxx+Ca sheet was also investigated. The Tafel polarization plots in Figure 3.24 showed that with increase in the sensitization time, the corrosion rates of the samples are similar, with a minor decrease of the corrosion potential, less than 100 mV as seen in Table 3.7. Such change could be due to increase in β-phase (Al_3Mg_2) with increase in holding sensitization time. If β-phase surrounds the grain continuously, it will result in severe intergranular corrosion. In the current study, changes in the Ca content do not show changes with corrosion behavior through with the increase in sensitization. Furthermore, corrosion rates between 5xxx+Ca H and rolled 5xxx+Ca showed comparable data. However, the extent of corrosion and its propagation vary microstructurally with the increase in sensitization time up to 50 hrs. The cross-section analysis of corroded rolled 5182 surfaces suggested that for 0 hr. sensitization, pitting corrosion seems to be dominant while for 50 and 100 hrs. samples, showed slight improvement and passivation in the 100 hrs. sample.

3.2 Microstructural Analysis

3.2.1 5xxx Al Alloys

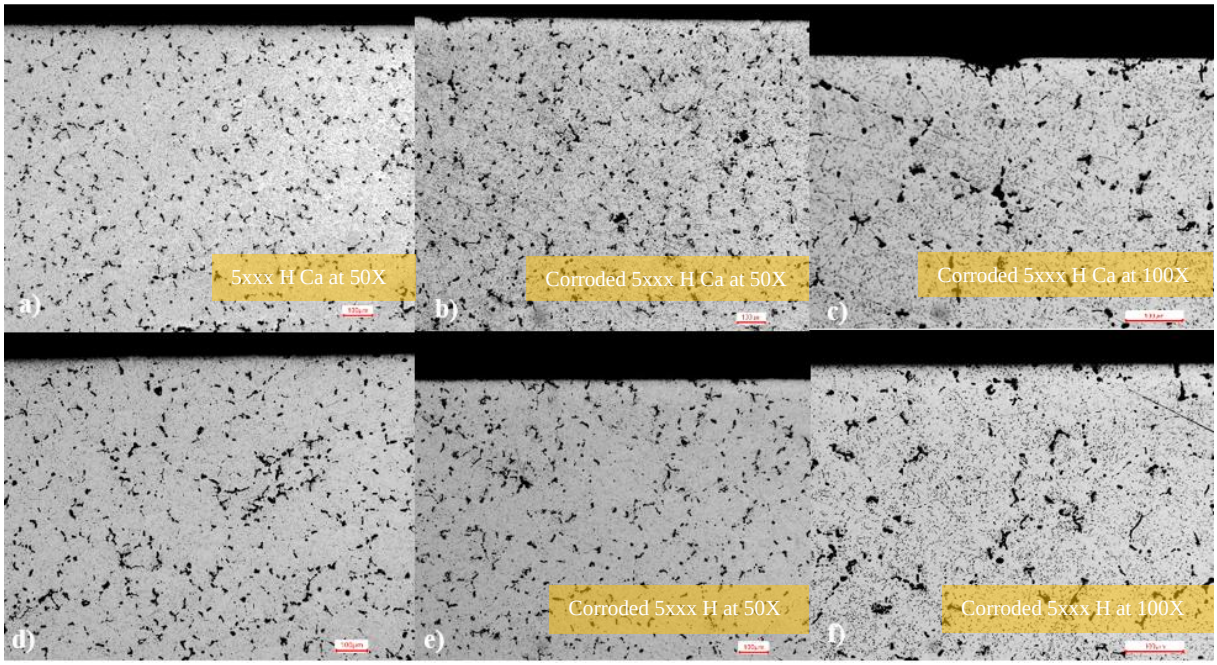

Figure 3.25: Cross-section images of **a)** 5xxx H Ca control surface **b-c)** corroded 5xxx H Ca **d)** 5xxx H control surface e-f) corroded 5xxx H surfaces.

The microstructure of homogenized 5xxx Al alloys with and without calcium can be seen in Figure 3.25. The 5xxx H Ca and 5xxx H alloys show minute pits and fine precipitates across the cross section while the grain boundaries are not distinct. Localized corrosion here can be seen to propagate through the continuation of fissures past the initial pit structure. While the size of the initial pits through Cl^- interaction varies throughout the 5xxx H Ca and 5xxx H alloys, the propagation is seen to be similar. The addition of trace Ca did not show significant changes in the microstructure in the homogenized 5xxx alloy.

Changes between the as-cast and homogenized alloys can be differentiated through the reduced number of precipitates in the as-cast alloy. Localized pitting corrosion was observed at the corrosion edge in both cases with propagation along the cell boundaries. Despite the changes in microstructure,

the corrosion behavior resonates with the homogenized alloy. In addition, any immediate changes due to addition of calcium could not be identified across the corroded surface.

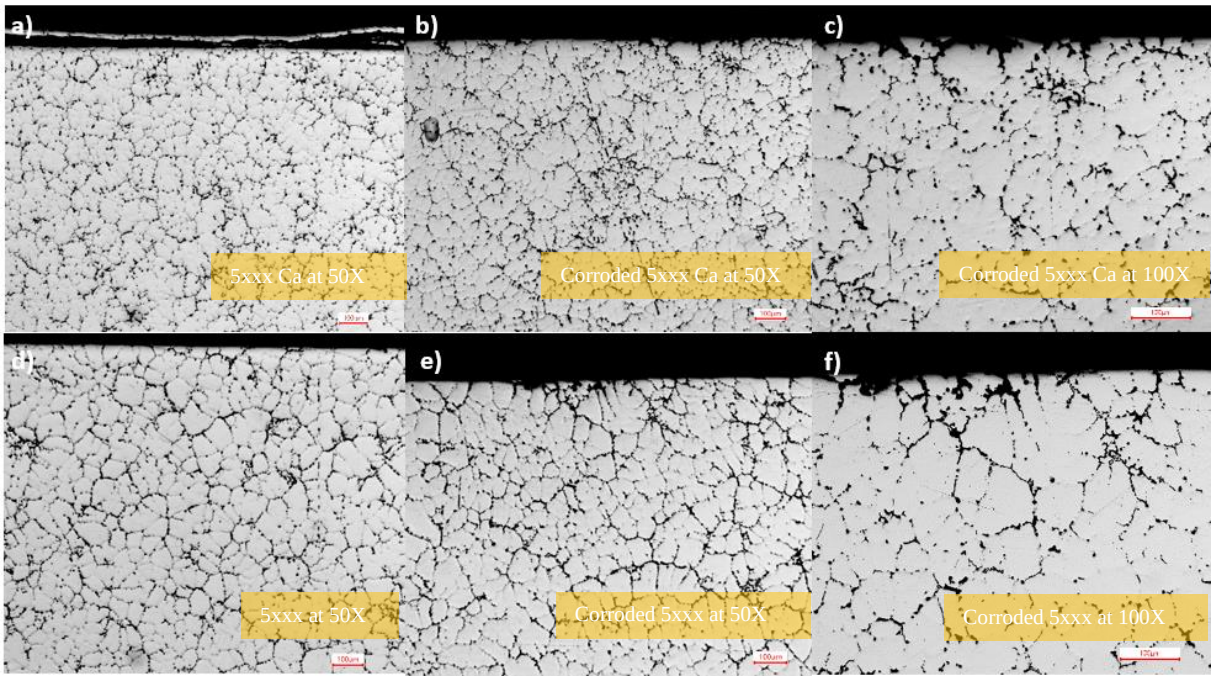

Figure 3.26: Cross-section images of **a)** 5xxx Ca control surface **b-c)** corroded 5xxx Ca **d)** 5xxx control surface **e-f)** corroded 5xxx surfaces.

3.2.2. 6xxx Al Alloys

The microstructure of homogenized 6xxx alloys with and without calcium are illustrated in Fig 41. The pitting continues in both homogenized alloys however no immediate effects of the addition of calcium can be seen. However, with homogenization, the microstructure in Figure 3.27 showed a contrast compared to as-cast 6xxx alloys. In the as-cast samples, the cell boundaries are more pronounced, showed less contrast and absence of precipitates within the cell structure.

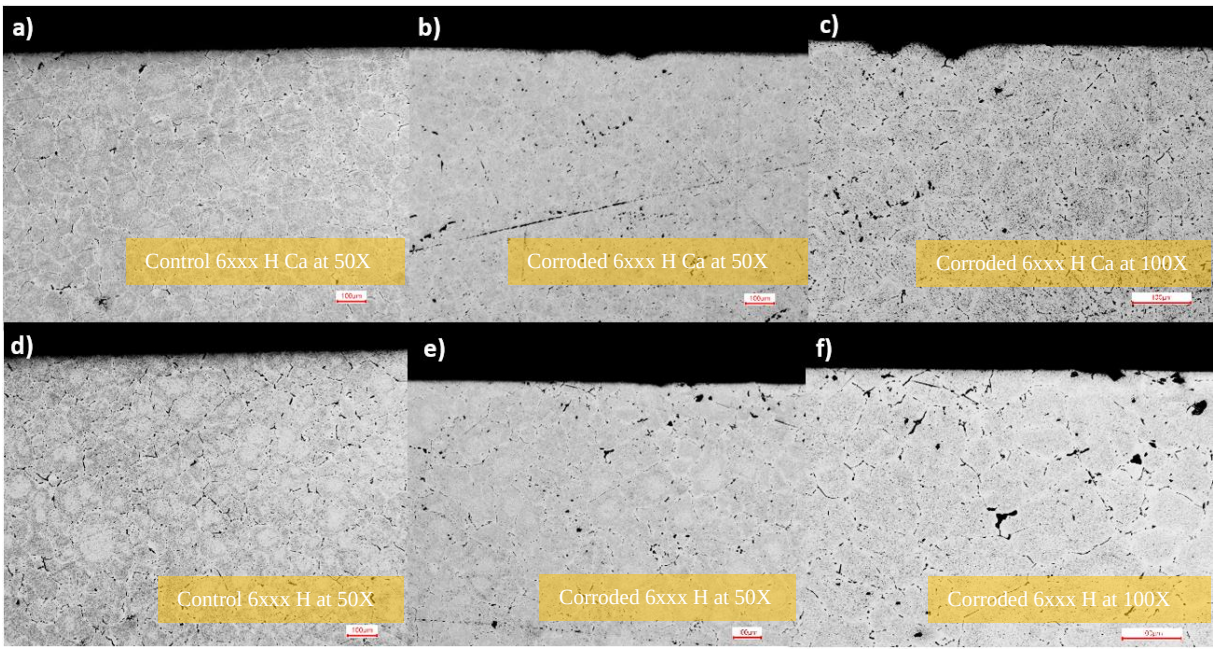

Figure 3.28: Cross-section images of **a)** 6xxx H Ca control surface **b-c)** corroded 6xxx H Ca **d)** 6xxx H control surface e-f) corroded 6xxx H surfaces.

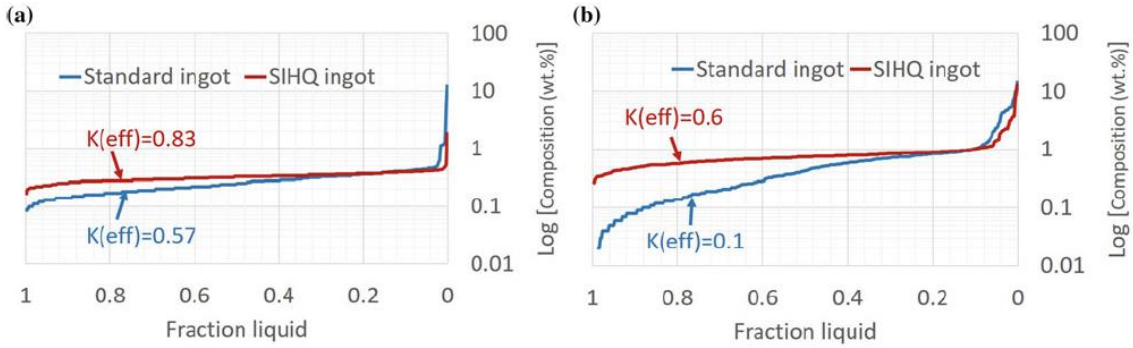

Figure 3.27: SEM EDS ordered composition of 6A position of standard and stirred in-situ homogenized ingots (SIHQ) for a) Mg, and b) Si elements [29].

The Figure 3.28 from reference [29] clearly shows the existence of microsegregation at equilibrium conditions of alloying elements, like Mg and Si, within a primary α-Al grain of an as-cast 6xxx alloy. The cooling curves from the 6A position (center of ingot) are chosen as the ingot isothermally stays in semi-solid region or near the equilibrium solidus temperature for a longer time before solidification. This allows increase in solidification time and promotes the formation of equilibrium phases. Figure 3.28 shows the reduction in microsegregation with the heat treatment seen from the difference in composition from the cell and cell boundary composition.

Images of the homogenized and as-cast samples are compared in Figure 3.29. The homogenized samples (Figure 3.29(a-c)) showed a contrasting difference between the center and the boundary of the grains/cells. The brighter region near the boundary are due to dispersoid or precipitate free zone. No such contrasting differences are noticed in the as-cast samples. In all the cases, the pitting corrosion was seen at the cross section of the corroded surface. In the as-cast 6xxx samples (Figure 3.29(d-f)), the pit seemed to initiate at the center of the cell/grain and propagate towards the cell/grain boundary. This is illustrated in Figure 3.30.

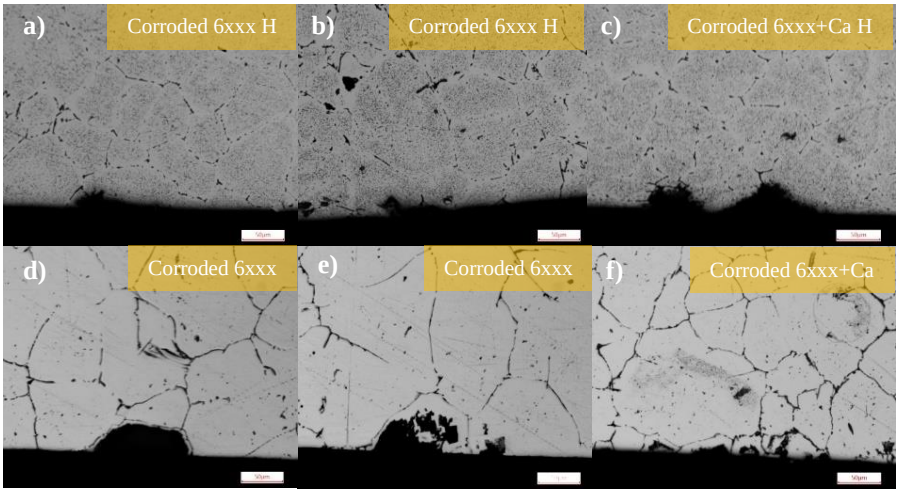

Figure 3.29: Cross-section images of corroded **a,b)** 6xxx H, **c)** 6xxx+Ca H, **d,e)** 6xxx, and **f)** 6xxx+Ca surfaces.

The inhomogeneity of Si and Mg distribution from the center to the edge of the grain may initiate the pitting attack and propagation in the cast alloy. Furthermore, the pitting behavior in the homogenized alloy showed pits near the cell boundary. As suggested by Figure 3.29 and Figure 3.39 in the following section, homogenization heat treatment not only reduces intermetallic particle fraction, particle size and microsegregation but also creates a particle free zone near the grain boundary. The result in particle free zone within aluminum adjacent to the grain boundary particle makes the particle free zone to be more anodic and easily attacked during corrosion, as noticed in Figure 3.29 of the homogenized samples.

Figure 3.30: Schematic of corrosion mechanism indicating pitting corrosion (pits indicated by dashed line) initiating **a)** center of the cell and propagating through the cell in as-cast alloy **b)** across the cell boundary in homogenized alloy.

3.2.3 Rolled 6xxx Al Alloys

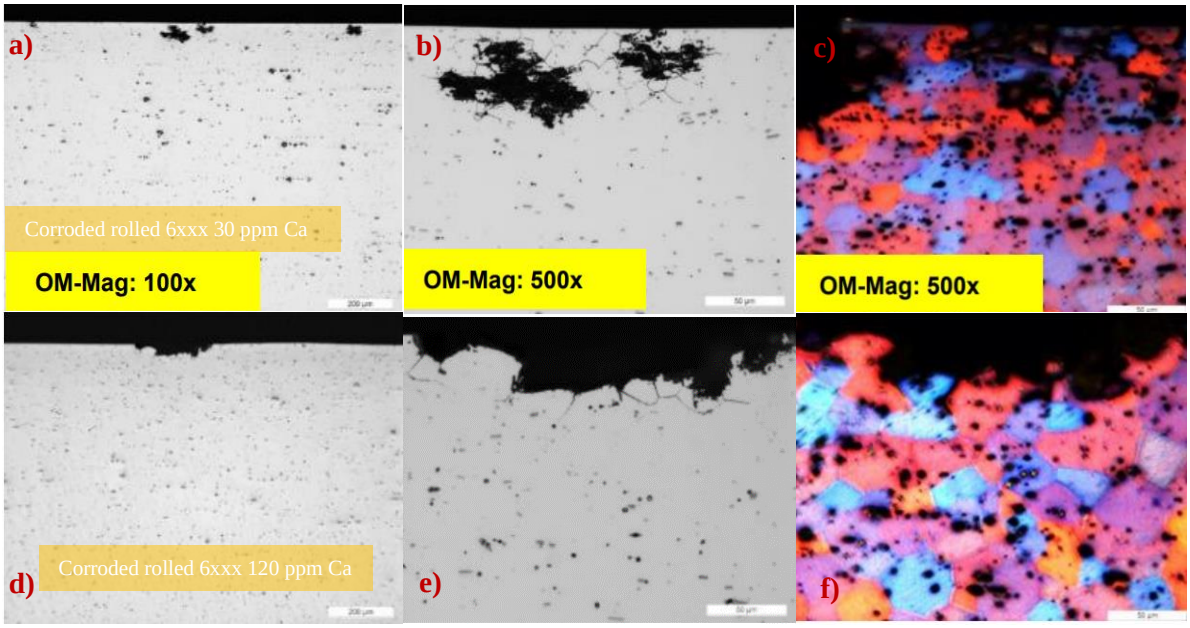

Figure 3.31: Cross-section images of **a)** corroded rolled 6xxx 30 ppm Ca at 100X **b)** corroded rolled 6xxx 30 ppm Ca at 500X **c)** (anodized) corroded rolled 6xxx 30 ppm Ca at 500X **d)** corroded rolled 6xxx 120 ppm Ca at 100X **e)** corroded rolled 6xxx 120 ppm Ca at 500X **f)** (anodized) corroded rolled 6xxx 120 ppm Ca at 500X.

The microstructure of rolled 6xxx with 30 ppm Ca and 120 ppm Ca are presented in Figure 3.31. The optical microscopy of the rolled 6xxx Al alloys showed the elongated grain structure. From the anodized images in Figure 3.31c and Figure 3.31f the pitting corrosion can be seen to across the corrosion edge and propagate across the grain boundary. This localized corrosion is much fewer with the alloy with higher Ca content from Figure 3.32 and images from the 3D profilometer in Figure 3.33. In addition, the diameter of the pit entry is much wider in the case of the rolled 6xxx at 120 ppm Ca, however the pit density is much larger in the 30 ppm Ca alloy as seen in Figure 3.32.

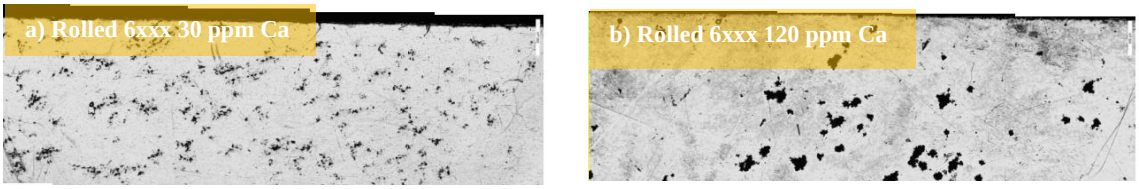

Figure 3.32: Corroded surface image of a) Rolled 6xxx 30 ppm Ca and b) Rolled 6xxx 120 ppm Ca [25].

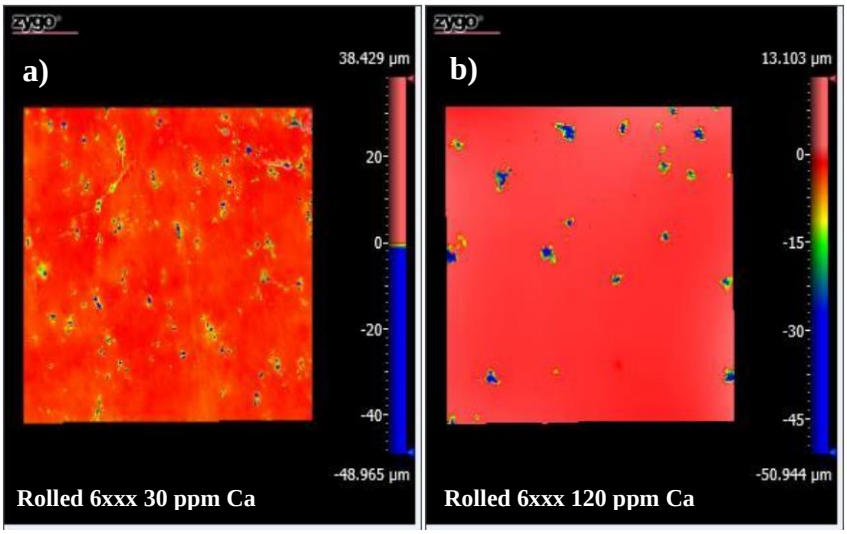

Figure 3.33: Corroded surface 3D profile of **a)** rolled 6xxx 30 ppm Ca **b)** rolled 6xxx 120 ppm Ca obtained through Zygo 3D Optical Profilometer [25].

3.2.3 Rolled 5xxx Al Alloys

The rolled 5xxx Al alloys was solution heat treated and sensitized at 0 hrs, 50 hrs, and 100 hrs. Figure 3.34 shows the microstructure of the as-received alloy without any additional homogenization. As-received rolled 5xxx show un-recrystallized grain structure while further heat-treated alloys showed re-crystallized grain structure.

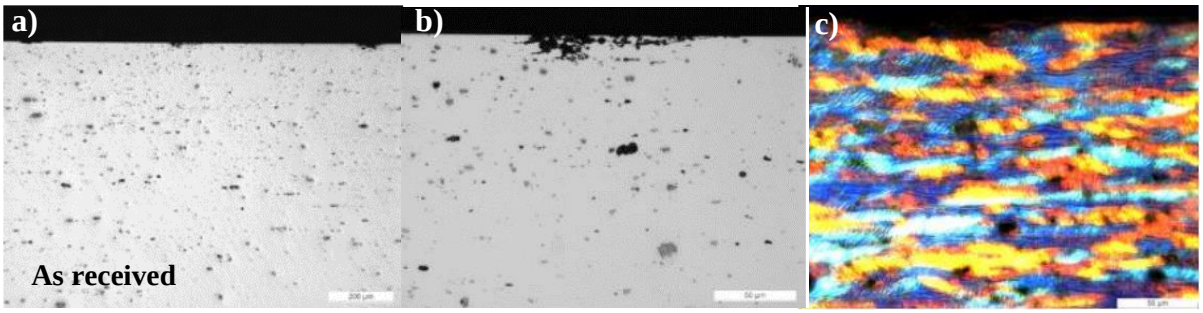

Figure 3.34: Cross-section images of **a)** rolled 5xxx as-received at 100 x **b)** corroded rolled 5xxx as-received at 500x **c)** anodized rolled 5xxx as-received at 500x [25].

The localized corrosion in the rolled 5xxx Al alloy at different sensitization times are shown in Figure 3.35. Recrystallized grains can be seen for the solution heat treated (SHT) alloys (450°C at 1 hr) and subsequently heat treated at 0 hr, 50 hrs and 100 hrs. No large variation is seen in the overall grain size with the different sensitization time. At 0 hrs. sensitization time, several pits of average depth 24 µm can be seen across the corroded edge. Larger and coarser pits are seen at the 0 hr sensitized alloy surface as seen in Figure 3.36a. However, at 50 hrs, the pitting continues increased pit depth ranging towards 40 µm. The nature of localized corrosion indicates increased pit density across the corrosion edges. At 100 hrs, the localized corrosion shows shallower pits across the corrosion surface as seen in Figure 3.35(g-i) and 3.36c. This agrees with the electrochemical studies in the previous section suggesting a slight improvement in the corrosion behavior compared to the alloys at other sensitized times.

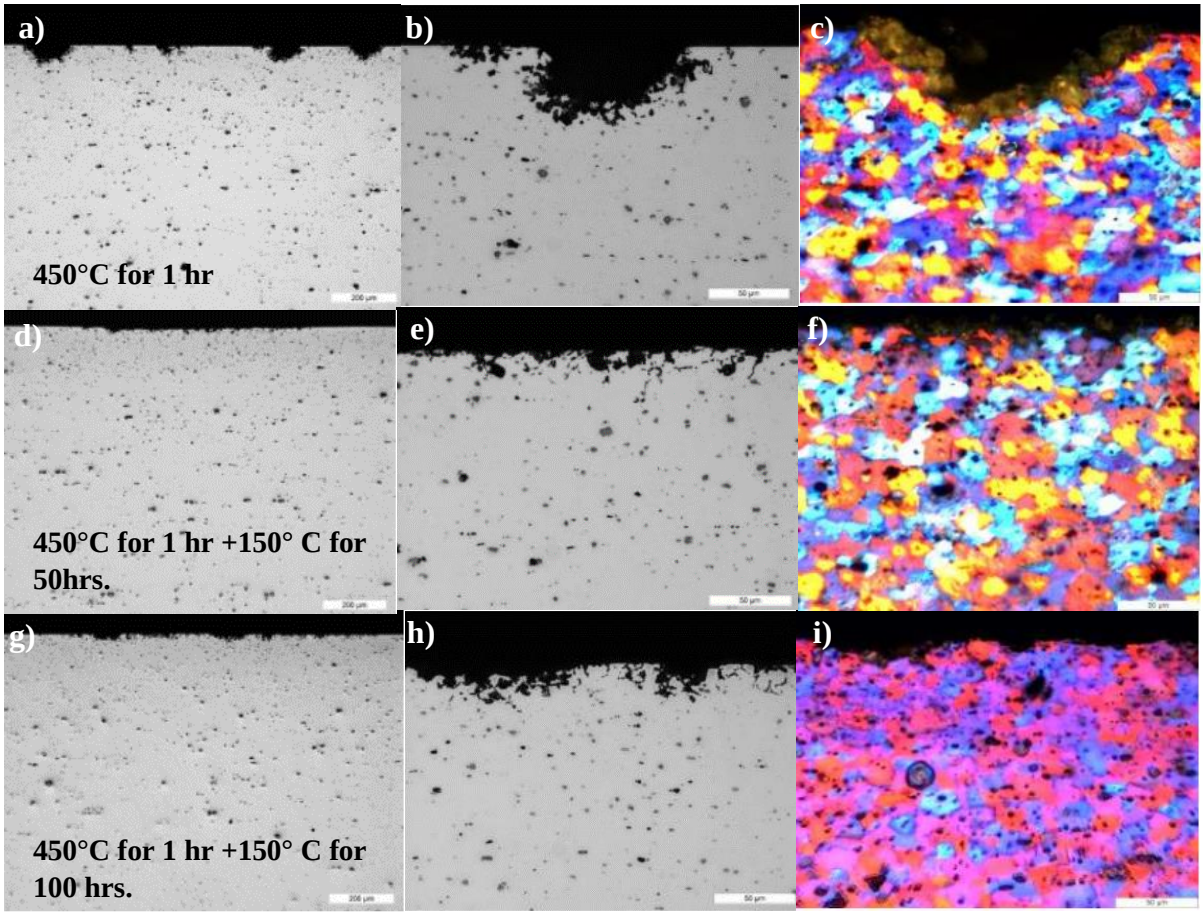

Figure 3.35: Cross-section images of **a)** rolled 5xxx 0 hrs. at 100x **b)** rolled 5xxx 0 hr. at 500x **c)** anodized rolled 5xxx 0 hr. at 500x **d)** rolled 5xxx 50 hrs. at 100x **e)** rolled 5xxx 50 hrs. at 500x f) anodized rolled 5xxx 50 hrs. at 500x hrs. **g)** rolled 5xxx 100 hrs. at 100x **h)** rolled 5xxx 100 hrs. at 500x **i)** anodized rolled 5xxx 100 hrs. at 500x hrs. *5xxx alloy solution heat treated (SHT) at 450°C for 1 hr. and heat treated at 150°C for 0 hr., 50 hrs., and 100 hrs.* [25].

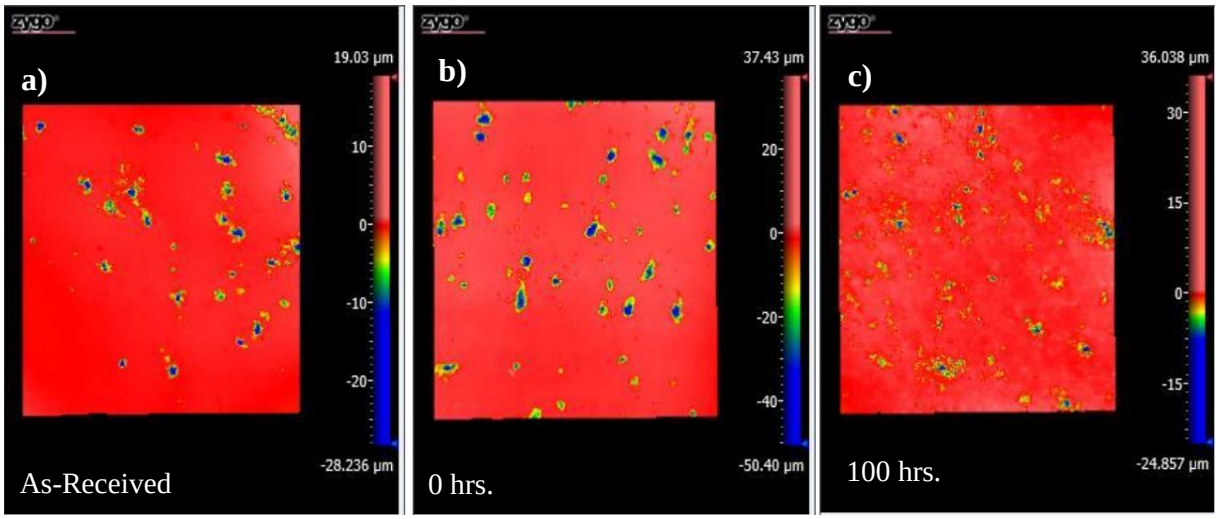

Figure 3.36: Corroded 3D profile of rolled 5xxx alloy at **a)** AR. **b)** 0 hrs. **c)** 100 hrs. 5xxx alloy solution heat treated (SHT) at 450°C for 1 hr and heat treated at 150°C for 0 hrs., 50 hrs., and 100 hrs. [25].

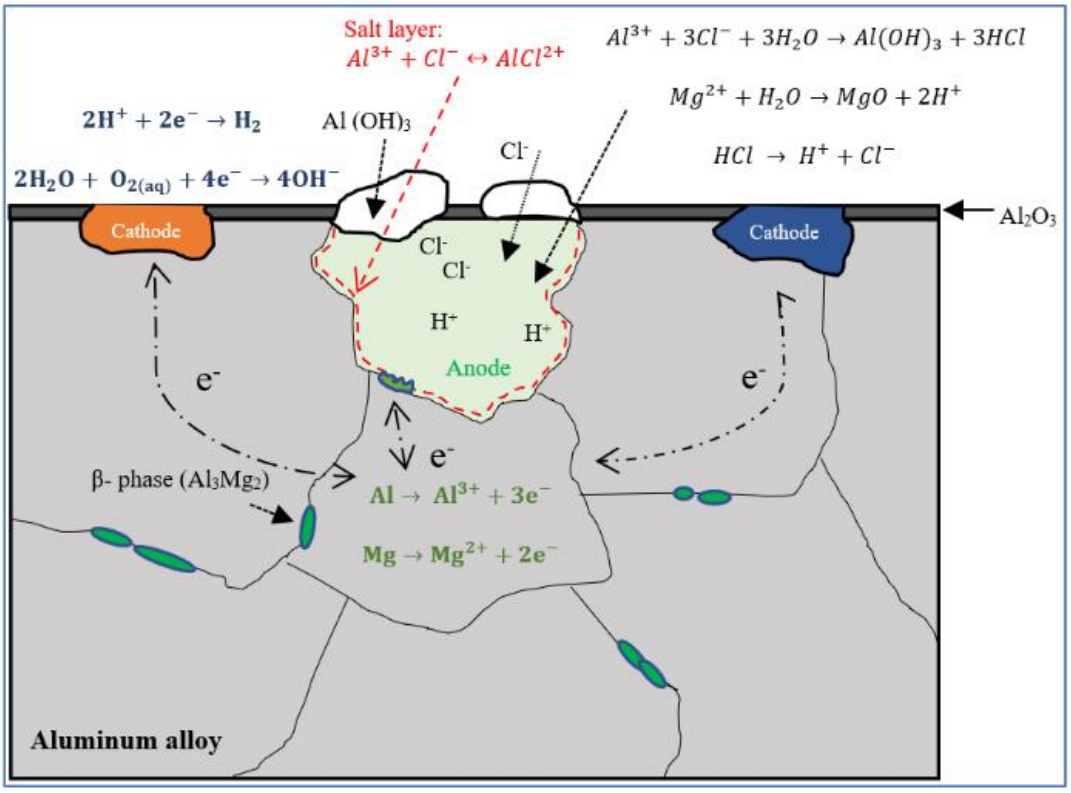

Figure 3.37: Schematic of anodic dissolution of Al_3Mg_2 (β-phase) during pitting corrosion.

The susceptibility of localized attack is attributed to the growth and sensitization of Al_3Mg_2 (β-phase) precipitates nucleating preferentially across the grain boundaries. Intermetallic compounds present in the matrix that are more noble, may act as cathodic sites. During the electrochemical reaction, increase in the cathodic area will promote the anodic dissolution of the β-phase and surrounding matrix. This leads to the cavity formation and subsequent corrosion around the grain boundaries. β-phase dissolution will then introduce metal cations, which increases the local pH and with the chloride environment, the local chemistry supports further decrease in the breakdown potential and increase in the overall dissolution rate. This chain of reactions can progress through the network of anodic phases near the grain boundaries [30,31]. The corrosion accelerates, in cases where the spread of the anodic phases is continuous along the grain boundary and leads to continuous IGC and subsequently grain fallout. Studies [31, 32] also revealed that β-phase can coarsen with longer periods of exposure, limiting spread along the grain boundaries.

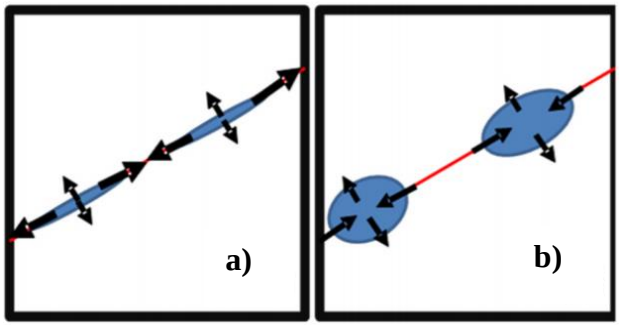

Figure 3.38: Schematic diagrams of precipitation evolution of β-phase when annealed **a)** Elongation stage **b)** Spheroidization stage [32].

Ding et. al. [32] discusses the evolution of β-phase in 5E83 alloy annealed at 210°C. As temperature is increased, the β-phase was seen to grow fast parallel to the GB and slowly in the perpendicular direction to form an ellipsoid figure which is labelled as the “elongation stage” (Fig 50a). During the second stage with prolonged annealing time, the β-phase precipitates are shown to grow thicker perpendicular to the GB (spheroidization stage in Figure 3.38b). Ding et. al. [32] suggested the improvement in corrosion resistance due to the coarsening effect.

At higher sensitization times, like in case of the 50 hrs, Cl^- interaction introduces structural damage through pitting reaching the grain boundaries while anodic dissolution of β-phase can coherently triggering IGC initiation and spreading. However, if the β-phase can coarsen at longer hours leading to a discontinuous spread across the grain boundary [31]. This discontinuity can limit the spread of anodic dissolution along the GB and improve overall corrosion resistance.

3.2.4 5xxx vs 6xxx Al Alloys

The polarized images in Figure 3.39, showed the equiaxed α-Al grains for as-cast and homogenized samples. The Ca addition to the 6xxx alloy changed the α-Al grain morphology to more globular, while the Ca addition to 5xxx alloy had no changes to the grain morphology but reduced the grain size slightly. As expected, homogenization removed the dendritic structure. In 6xxx alloy, Ca addition increased the intermetallic particle size (Figure 3.39) of the as-cast sample, while no difference is seen in 5xxx alloy. The impact of homogenization on refining intermetallic particles is larger for 6xxx alloy. The total number of particles per square area (Figure 3.39) have reduced with homogenization for 5xxx alloy.

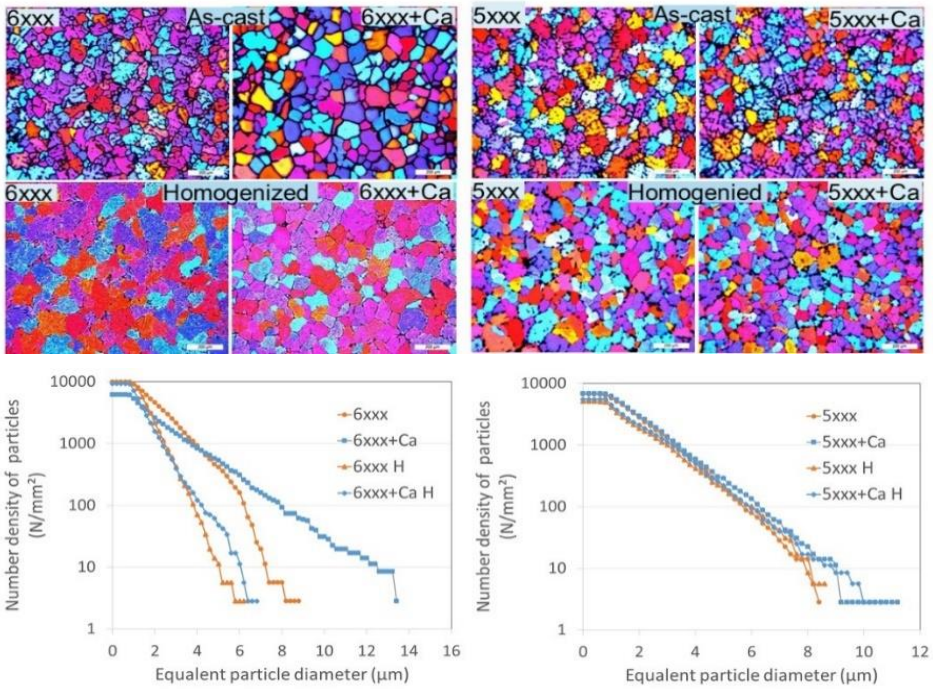

Figure 3.39: Polarized light microscopy images showing α-Al grain structures, and statistics describing the intermetallics size distribution [25].

The thermodynamic phase calculation (Figure 3.5) predicts in addition to the primary α-Al: (a) α-AlFeSi and β-AlFeSi forming from liquid in 6xxx alloy, and (b) $Al_6(FeMn)$ and Mg_2Si forming from liquid in 5xxx alloy. The thermodynamic calculation also predicts Al_2Si_2Ca forming from liquid in 6xxx+Ca alloy.

Here both, 5xxx and 6xxx Al alloys, showed the effects of localized corrosion. Based on the corroded cross-sectional analysis, corrosion in 6xxx alloys are dominated by pitting corrosion. In

general, once the surface passive layer of the Al break, the Cl^- is exposed to the metal surface where pitting are seen to initiate at electroactive sites [4,33]. The as-cast samples have more cathodic intermetallic at the grain boundary, such as Fe intermetallics, which results in anodic dissolution of the matrix. Alternatively, the homogenized sample showed pit at the particle free zone near the cell boundary. The distribution of cathodic sites such as Si and Mg_2Si accelerate the anodic dissolution along the particle free zones. If the cathodic area is greater than the anodic, there is an increase in the electrochemical activity and anodic current density leading to a greater anodic dissolution of the bulk metal [34]. In the case of 5xxx alloy, the corrosion type was seen to be localized in the form of pitting corrosion. The 5xxx alloys with the presence of higher Mg content lead to consequent corrosion due to β-phase formation along the grain boundary. The presence of Cl^- initiated pitting at electronegative sites, and corrosion progresses through anodic dissolution. The electron transfer within the cathodic sites, such as β-phase (anodic to Al matrix) in case of 5xxx, may have propagated the pit structure to the grain boundary and introduced localized corrosion.

There was no change in the corrosion rate of 6xxx alloy, irrespective of addition of Ca or heat treatment. However, the microstructural changes produced by homogenization heat treatment showed that as-cast 6xxx to have greater susceptibility to localized corrosion. An increase in intermetallic size in as-cast condition may have influenced the size of cathodic sites. During the corrosion process, larger areas of cathodic sites in the as-cast alloys as suggested by Figure 3.29 must accelerate the electrochemical activity during pitting. This would explain the increased propensity to localized corrosion for as-cast 6xxx as suggested by Figure 3.16. While addition of Ca showed changes in intermetallic sizes for as-cast 6xxx, the corrosion effects are comparable due to similar electrochemical behavior and corrosion mechanism. The size and electrochemical activity of the intermetallics after addition of Ca needs further investigation to understand its influence in corrosion behavior.

Chapter 4: Conclusions

The effects of trace amount of Ca on corrosion properties of homogenized and as-cast 5xxx and 6xxx Al alloys were studied. Using electrochemical techniques, the electrochemical framework and corrosion response of the 5xxx and 6xxx Al alloys to a specific environment, chloride containing solution was established. The electrochemical and microstructural studies lead to the following conclusions:

- *Electrochemical studies:*

1. Corrosion of 5xxx and 6xxx Al alloys series were studied in sea water environment.
2. These alloys were studied in as-cast and homogenized (sensitized) conditions.
3. It was found that the alloys were susceptible to localized corrosion called pitting corrosion.
4. 5xxx Al alloy showed improved corrosion behavior compared to 6xxx alloys in the chloride environment.
5. The role of trace amount of Ca in both alloys was also examined. Trace amount of Ca did not alter corrosion rate significantly, which was verified by cyclic polarization.
6. Although trace amount of Ca did not have profound effect on corrosion, it had a profound effect on microstructure of studied alloys.
7. 5xxx as-cast Al alloys showed improved passivity (corrosion) due to lower precipitation of secondary phases (intermetallics) compared to homogenized 5xxx Al alloys. Increase in secondary phase particles can disrupt the oxide layer and introduce micro-galvanic corrosion within the alloy.
8. Changes in pH was shown to influence the passivity of the alloy. Characteristic potentials such as E_{pit} and E_{ptp} are seen to be independent of pH.
9. 6xxx as-cast Al alloys showed increase in intermetallic size which increased the susceptibility to localized corrosion compared to 6xxx homogenized Al alloys.
10. With respect to the effect of atmosphere, pure O_2 had detrimental effect on the formation of the passive film (not present). However, it had no effect on the repassivation stage (regardless of the atmosphere).

11. The corrosion behavior of rolled 5xxx and 6xxx alloys were close to the cast 5xxx and 6xxx alloys. Changes in sheet thickness did not affect the overall corrosion behavior.
12. The effect of heat treatment (sensitization) was studied only on 5xxx Al alloys. Only the prolonged (100 hrs.) heat treatment showed improved effect on corrosion.

- *Microstructural studies:*

1. 5xxx alloys showed pitting corrosion and propagation across the cell boundaries.
2. Pitting corrosion initiates near the center of the cell in as-cast 6xxx alloys. With respect to the homogenized alloys, pitting corrosion initiates near cell boundaries (free from the intermetallics) whereas in the as-cast alloy, corrosion initiates near the center of the cell. This is attributed to the inhomogeneity of Si and Mg distribution leads to an electrochemical difference during the pitting process.
3. Rolled 6xxx Al alloys with 120 ppm Ca showed fewer pits with wider diameter of the pit entry compared to the rolled 6xxx at 30 ppm Ca alloy.
4. Sensitization time affects the pitting corrosion via the morphology of β-phase. Up to 50 hrs. β-phase is randomly distributed throughout the Al alloy matrix. Longer sensitization times lead to coarsening of β-phase (fewer in number) causing the reduction of corrosion rate.

Future Work

1. As previously discussed in the earlier chapters, the presence of trace calcium up to 50 ppm did not show significant changes in the corrosion rate. However, from microstructural studies, addition of trace calcium showed changes in the grain morphology in the 6xxx alloy. The addition of 120 ppm Ca in rolled alloys also showed decrease in the pit density with wider pit diameter compared to 30 ppm Ca. Increasing Ca content has shown to influence the corrosion behavior. Additional studies with higher calcium addition can be studied to further evaluate the calcium behavior.

2. Heat treatment and compositional changes have shown to influence the intermetallic formation in Al alloys. The mechanical properties of the Al alloy also depend on the volume fraction and size of secondary particles. Therefore, further detailed characterization on the formation, volume fraction and size of electroactive intermetallic particles such as Mg_2Si, β-phase that also take part in the corrosion process would give a qualitative understanding with the aim to improve the mechanical properties while mitigating the corrosion extent.

3. From chapter 3, the changes in microstructure between as-cast, homogenized and rolled alloys can showed differences in the corrosion resistance. In addition, the formation of the protective passive film depends on the composition and fabrication process. To improve the initial passivity of the alloy surface, additional research with applications of coatings and further thermomechanical processing can be beneficial.

References

1. Hirsch J (2014) Recent development in aluminum for automotive applications. T. Nonferr. Metal Soc. 24(7):1995-2002. doi:10.1016/s1003-6326(14)63305-7.

2. Kumari SS, Pillai RM, Pai BC, Nogita K, Dahle AK (2006) Influence of calcium on the microstructure and properties of an Al-7Si-0.3Mg-xFe alloy. Metall. Mater. Trans. A 37(8):2581-2587. doi:10.1007/bf02586230.

3. Jones, D. A. (1996). Principles and prevention of corrosion. Upper Saddle River, NJ: Prentice-Hall.

4. Natishan, P. M., & O'Grady, W. E. (2014). Chloride Ion Interactions with Oxide-Covered Aluminum Leading to Pitting Corrosion: A Review. Journal of The Electrochemical Society, 161(9). doi: 10.1149/2.1011409jes

5. Yasakau, K., Zheludkevich, M., & Ferreira, M. (2018). Role of intermetallics in corrosion of aluminum alloys. Smart corrosion protection. Intermetallic Matrix Composites, 425–462. doi: 10.1016/b978-0-85709-346-2.00015-7

6. Szklarska-Smialowska, Z. (1999). Pitting corrosion of aluminum. Corrosion Science, 41(9), 1743–1767. doi: 10.1016/s0010-938x(99)00012-8

7. Sun, Q., & Chen, K. (2018). Inflection of backward sweep of cyclic polarization curve: Pit transition potential E ptp. Materials and Corrosion, 69(12), 1729-1740. doi:10.1002/maco.201810419

8. Zhu, J., & Hihara, L. (2010). Corrosion of continuous alumina-fibre reinforced Al–2 wt.% Cu–T6 metal–matrix composite in 3.15 wt.% NaCl solution. Corrosion Science, 52(2), 406–415. doi: 10.1016/j.corsci.2009.09.028

9. Trueba, M., & Trasatti, S. P. (2015). Electrochemical approach to repassivation kinetics of Al alloys: Gaining insight into environmentally assisted cracking. Corrosion Reviews, 33(6), 373-393. doi:10.1515/corrrev-2015-0054

10. Shukla, P. (2008). Thermodynamics of corrosion and potentiometric methods for measuring localized corrosion. Techniques for Corrosion Monitoring, 156-186. doi:10.1533/9781845694050.1.156

11. Yasuda, M. (1990). Pitting Corrosion of Al and Al-Cu Single Crystals. Journal of The Electrochemical Society, 137(12), 3708. doi: 10.1149/1.2086291

12. Cicolin D, Trueba M, Trasatti S (2014) Effect of chloride concentration, pH and dissolved oxygen, on the repassivation of 6082-T6 Al alloy. Electrochim. Acta 124:27-35. doi: 10.1016/j.electacta.2013.09.003.

13. Pickering, H. W. (1986). Whitney Award Lecture—1985: On the Roles of Corrosion Products in Local Cell Processes. Corrosion, 42(3), 125–140. doi: 10.5006/1.3584892

14. Ferri, M., Trueba, M., Trasatti, S. P., Cabrini, M., & Conte, A. L. (2017). Electrochemical investigation of corrosion and repassivation of structural aluminum alloys under permanent load in bending. *Corrosion Reviews, 35*(4-5), 225-239. doi:10.1515/corrrev-2017-0068

15. Trueba M, Trasatti SP (2010) Study of Al alloy corrosion in neutral NaCl by the pitting scan technique. Mater. Chem. Phys. 121(3):523-533. doi: 10.1016/j.matchemphys.2010.02.022.

16. Lim ML, Kelly R, Scully J (2015) Overview of intergranular corrosion mechanisms, phenomenological observations, and modeling of AA5083. Corrosion 72(2):198-220. doi:10.5006/1818.

17. Zeng F, Wei Z, Li J, Li C, Tan X, Zhang Z, Zheng Z (2011) Corrosion mechanism associated with Mg2Si and Si particles in Al–Mg–Si alloys. T. Nonferr. Metal Soc. 21(12):2559-2567. doi:10.1016/s1003-6326(11)61092-3.

18. Ramachandran DC, Murugan SP, Kim YM, Kim D, Kim GG, Nam DG, Park YD (2019) Effect of Microstructural Constituents on Fusion Zone Corrosion Properties of GMA Welded AA 5083

with Novel Al–Mg Welding Wires of High Mg Contents. Met. Mater. Int., 1341-1353. doi:10.1007/s12540-019-00434-9

19. Choi I, Cho S, Kim S, Jo Y, Kim S (2018) Improved corrosion resistance of 5XXX aluminum alloy by homogenization heat treatment. Coatings 8(1):39. doi:10.3390/coatings8010039

20. Kumari, S. S., Pillai, R., & Pai, B. (2008). Structure and properties of calcium and strontium treated Al–7Si–0.3Mg alloy: A comparison. Journal of Alloys and Compounds, 460(1-2), 472-477. doi:10.1016/j.jallcom.2007.05.085

21. Ludwig TH, Schaffer PL, Arnberg L (2013) Influence of some trace elements on solidification path and microstructure of Al-Si foundry alloys. Metall. Mater. Trans. A 44(8):3783-3796. doi:10.1007/s11661-013-1694-y.

22. Lim ML, Kelly R, Scully J (2015) Overview of intergranular corrosion mechanisms, phenomenological observations, and modeling of AA5083. Corrosion 72(2):198-220. doi:10.5006/1818.

23. Gupta RK, Zhang R, Davies CHJ, Birbilis N (2014) Theoretical study of the influence of microalloying on sensitization of AA5083 and moderation of sensitization of a model Al-Mg-Mn alloy via Sr additions. Corrosion 70(4):402-413. doi: 10.5006/1117.

24. Flores, J. R. (2006). The role of magnesium in the electrochemical behaviour of 5XXX aluminium-magnesium alloys (Unpublished doctoral dissertation). Diss. Delft.

25. Metallographic results provided by Dr. Kumar Sundaram from Novelis Inc.

26. Zeng F, Wei Z, Li J, Li C, Tan X, Zhang Z, Zheng Z (2011) Corrosion mechanism associated with Mg2Si and Si particles in Al–Mg–Si alloys. T. Nonferr. Metal Soc. 21(12):2559-2567. doi:10.1016/s1003-6326(11)61092-3.

27. Ramachandran DC, Murugan SP, Kim YM, Kim D, Kim GG, Nam DG, Park YD (2019) Effect of Microstructural Constituents on Fusion Zone Corrosion Properties of GMA Welded AA 5083

with Novel Al–Mg Welding Wires of High Mg Contents. Met. Mater. Int., 1341-1353. doi:10.1007/s12540-019-00434-9

28. Comotti, I. M., Trueba, M., & Trasatti, S. P. (2013). The pit transition potential in the repassivation of aluminium alloys. Surface and Interface Analysis, 45(10), 1575-1584. doi:10.1002/sia.5270

29. Kumar S, Cracroft J, Wagstaff RB (2020) Influence of liquid jet stirring and in-situ homogenization on the intermetallics formation during DC casting of a 6xxx Al alloy rolling ingot. Light Met. 2020 1013-1018. doi:10.1007/978-3-030-36408-3_137.

30. Li, Y., Cai, J., Guan, L., & Wang, G. (2019). PH-dependent electrochemical behaviour of Al3Mg2 in NaCl solution. Applied Surface Science, 467-468, 619-633. doi:10.1016/j.apsusc.2018.10.193

31. Lim ML, Kelly R, Scully J (2015) Overview of intergranular corrosion mechanisms, phenomenological observations, and modeling of AA5083. Corrosion 72(2):198-220. doi:10.5006/1818.

32. Ding, Y., Gao, K., Huang, H., Wen, S., Wu, X., Nie, Z., Zhou, D. (2019). Nucleation and evolution of β phase and corresponding intergranular corrosion transition at 100–230 °C in 5083 alloy containing Er and Zr. Materials & Design, 174, 107778. doi:10.1016/j.matdes.2019.107778

33. Natishan PM, O'Grady WE (2014) Chloride ion interactions with oxide-covered Aluminum leading to pitting corrosion: a review. J. Electrochem. Soc. 161(9):c451-c432. doi: 10.1149/2.1011409jes.

34. Yasakau K, Zheludkevich M, Ferreira M (2018) Role of intermetallics in corrosion of aluminum alloys. Smart corrosion protection. Intermetallic Matrix Composites, 425–462. doi: 10.1016/b978-0-85709-346-2.00015-7

Appendix

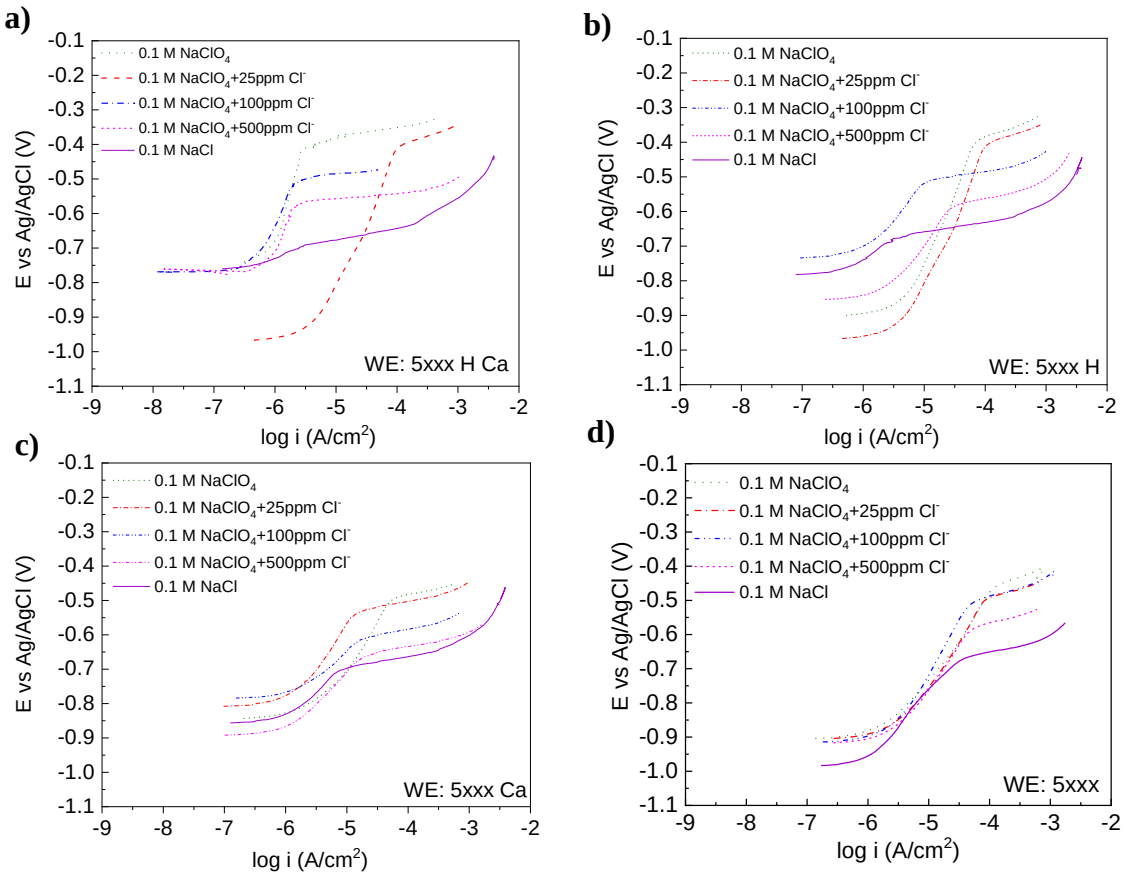

Figure A.1: Anodic Polarization of 5xxx alloys with varying concentrations of Cl^-.

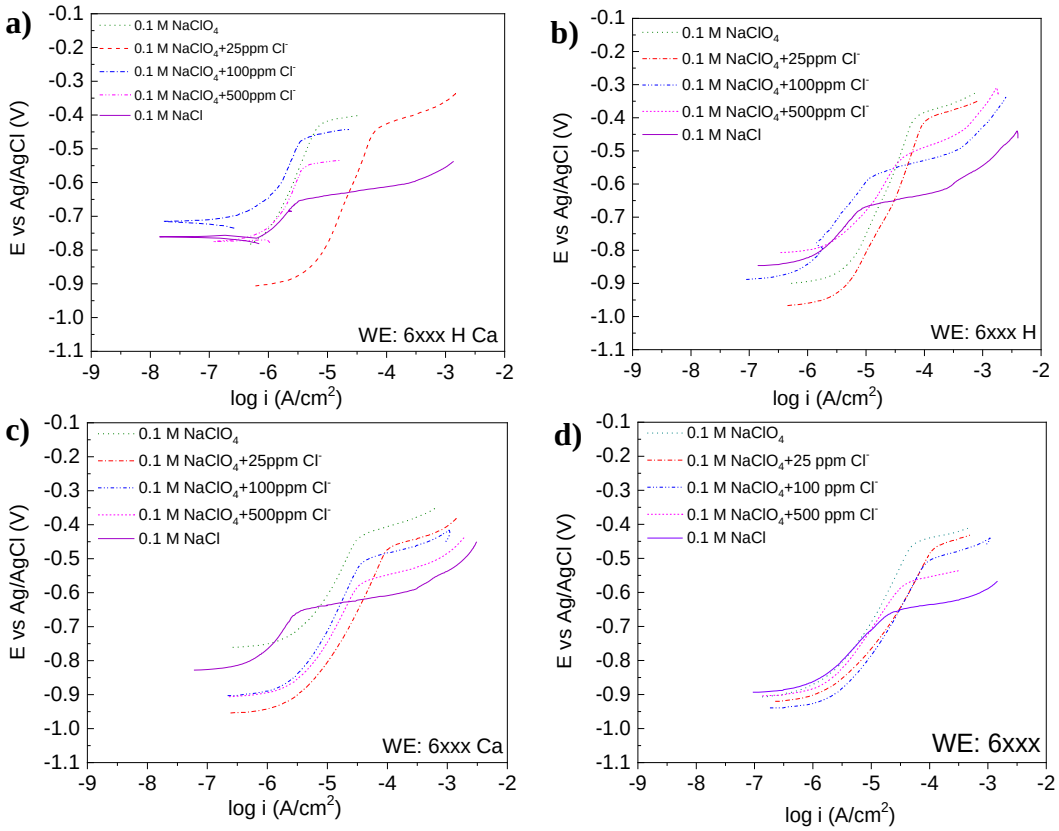

Figure A.2: Anodic Polarization of 6xxx alloys with varying concentrations of Cl^-.

Table A.1: Variation in breakdown potential with increasing ppm of Cl^- in 5xxx and 6xxx alloys.

Alloy	Concentration (ppm Cl^-)	E_{pit} (V)	Alloy	Concentration (ppm Cl^-)	E_{pit} (V)
6xxx H Ca	0	-0.4210	5xxx H Ca	0	-0.4000
	25	-0.4280		25	-0.4010
	100	-0.4760		100	-0.5090
	500	-0.5470		500	-0.5720
	3558 (0.1 M NaCl)	-0.6471		3558 (0.1 M NaCl)	-0.6900
	10674 (0.3 M NaCl)	-0.6600		10674 (0.3 M NaCl)	-0.7060
	21348 (0.6 M NaCl)	-0.7216		21348 (0.6 M NaCl)	-0.7210
6xxx H	0	-0.3860	5xxx H	0	-0.3970
	25	-0.4030		25	-0.4060
	100	-0.5070		100	-0.5125
	500	-0.5720		500	-0.5800
	3558 (0.1 M NaCl)	-0.6690		3558 (0.1 M NaCl)	-0.6760
	10674 (0.3 M NaCl)	-0.6890		10674 (0.3 M NaCl)	-0.7020
	21348 (0.6 M NaCl)	-0.7020		21348 (0.6 M NaCl)	-0.7440
6xxx Ca	0	-0.4232	5xxx Ca	0	-0.4886
	25	-0.4653		25	-0.5360
	100	-0.5010		100	-0.6090
	500	-0.5630		500	-0.6650
	3558 (0.1 M NaCl)	-0.6510		3558 (0.1 M NaCl)	-0.7090
	10674 (0.3 M NaCl)	-0.6840		10674 (0.3 M NaCl)	-0.7210
	21348 (0.6 M NaCl)	-0.6940		21348 (0.6 M NaCl)	-0.7350
6xxx	0	-0.4505	5xxx	0	-0.4543
	25	-0.4700		25	-0.4660
	100	-0.5140		100	-0.5001
	500	-0.5710		500	-0.5827
	3558 (0.1 M NaCl)	-0.6585		3558 (0.1 M NaCl)	-0.6724
	10674 (0.3 M NaCl)	-0.6870		10674 (0.3 M NaCl)	-0.6940
	21348 (0.6 M NaCl)	-0.7140		21348 (0.6 M NaCl)	-0.7400